This is a preprint, the final version is subject to change, of the American Mineralogist (MSA)
Cite as Authors (Year) Title. American Mineralogist, in press.
(DOI will not work until issue is live.) DOI: http://dx.doi.org/10.2138/am-2016-5442

1 **REVISION 1**

2

3 # Crystallographic orientation relationships in host–inclusion systems: new
4 # insights from large EBSD datasets

5

6 **Griffiths, Thomas A.**[1*] (th.griffiths@univie.ac.at)**, Habler, Gerlinde**[1]
7 (gerlinde.habler@univie.ac.at) **& Abart, Rainer** [1] (rainer.abart@univie.ac.at)

8 [1]Department of Lithospheric Research, Center for Earth Sciences, University of Vienna,
9 Althanstrasse 14, 1090 Vienna, Austria.

10 [*]corresponding author

11

12

13

14

15

16

17

18

19

20

21

22

Abstract

Crystallographic orientation relationships (CORs) between mineral inclusions and their hosts could potentially deliver information about inclusion formation processes and conditions. Most previous studies are based on small numbers of analyses. This paper uses EBSD to study host–inclusion CORs in an inclusion-rich Permian metapegmatite garnet (Koralpe region, Eastern Alps, Austria), demonstrating the importance of large datasets and of EBSD in particular for the analysis of CORs. The distribution of measured orientations reflects host garnet point group symmetry for 89% of inclusions analyzed (total N = 530). Each inclusion phase (rutile, corundum and ilmenite) shows at least three different CORs to host garnet. 'Statistical' CORs are introduced to describe distributions of inclusion orientations that have one or two degrees of freedom with respect to the host, but still reflect host crystal symmetry. Two end member characteristics of statistical CORs are distinguished: rotation and dispersion. Most statistical CORs observed show a mixture of both. Each inclusion phase shows at least one statistical COR. Multiple coexisting CORs and statistical CORs are not restricted to rutile. Re-examination of previous garnet–rutile COR studies in light of the new results indicates that COR information may have been overlooked when using small datasets. Variation in COR parameters correlates with broad differences in assumed metamorphic conditions for new and literature samples, suggesting that petrogenetic information may be available if COR formation can be understood. The favorability of the detected CORs cannot be explained by a simple model involving minimization of misfit between lattice planes, implying that other interface properties or the inclusion formation mechanism are important controls on COR development.

Introduction

Crystalline mineral inclusions can provide valuable information about the formation and evolution of rocks. The origins of inclusions determine the processes about which they can record petrological information and how this information is encoded, assuming changes in the properties of interest due to re-equilibration can be excluded. In some cases, just determining the origin of a population of inclusions can have important implications for the inferred tectonometamorphic history of a sample (e.g. Green II et al. 1997; Van Roermund et al. 2000; Ye et al. 2000; Mposkos and Kostopoulos 2001; Zhang and Liou 2003; Zhang et al. 2011; Ague and Eckert Jr. 2012; Ruiz-Cruz and Sanz de Galdeano 2013; Gou et al. 2014; Glassley et al. 2014).

Many approaches to inferring inclusion origins have been taken. All studies cited in this introduction consider the phases present, their compositions, distributions, shapes and any shape-preferred orientations. Some studies also include inclusion-based microstructures (Burton 1986; Perchuk 2008; Hwang et al. 2011, 2013, 2015), compositional zoning or diffusion profiles in inclusions or hosts (Burton 1986; Ague and Eckert Jr. 2012; Hwang et al. 2013; Khisina et al. 2013), and crystallographic orientation relationships (CORs) between inclusion and host crystallographic directions (Brearley and Champness 1986; Hwang et al. 2007, 2011, 2013, 2015; Zhang et al. 2011; Proyer et al. 2013, Xu et al. 2015).

CORs have mostly been used to try to confirm exsolution origins for inclusions, due to the assumption that ‘specific’ CORs (where the crystallographic orientation of one phase is fixed relative to another) are a diagnostic criterion for exsolution (e.g. Hwang et al. 2007). However, there is a lack of agreement about criteria to distinguish between host–inclusion CORs of different origins. Combined with other observations, different specific CORs have been

67 considered evidence both for (Hwang et al. 2011; Zhang et al. 2011) and against (Hwang et al.
68 2011, 2013, 2015) exsolution origins, and other authors have argued absence of a specific COR
69 does not rule out inclusion formation by exsolution (Brearley and Champness 1986; Ague and
70 Eckert Jr. 2012; Proyer et al. 2013; Xu et al. 2015).

71 Identification of inclusion origins in a sample via CORs is based on two assumptions:

72 1) The dataset obtained gives a representative picture of the distribution of inclusion
73 crystallographic orientations. The CORs defined from this distribution (and the relative
74 frequencies thereof) accurately represent the likelihood of finding an inclusion with a
75 given crystallographic orientation relative to the host.
76 2) The number, relative frequencies and characteristics of CORs developed during different
77 inclusion formation processes are known and distinguishable.

78 Assumption 2) requires that assumption 1) was fulfilled for any samples used to develop this
79 knowledge, thus assumption 1) is fundamental to the determination of inclusion origins.
80 However, many studies use only a few tens of inclusion orientations per sample to conclude
81 which - or whether - CORs are present.

82 The ability of electron backscatter diffraction (EBSD) to rapidly acquire large numbers of
83 crystallographic orientations has been exploited to obtain crystallographic orientations of rutile,
84 corundum and ilmenite inclusions (total N = 530) in two metapegmatite garnet host grains. Using
85 the new dataset this paper addresses the problem of how to accurately and representatively
86 characterize the distribution of inclusion crystallographic orientations using CORs. It then
87 discusses the potential of well-characterized sets of CORs to reveal the origins of inclusions,

88 answer wider petrogenetic questions and shed light on the lattice-scale mechanisms controlling
89 COR development.

90 Geological setting

91 The new dataset originates from metapegmatite garnets from the locality Wirtbartl, in the
92 Koralpe region, Austria (sample number: 04T26K, geographic coordinates: 5177709 N, 504737
93 E; UTM zone 33N, geodetic datum: WGS84). The Wirtbartl metapegmatites are intercalated
94 with metapelitic rocks of the Austroalpine Saualpe-Koralpe crystalline basement complex
95 (Schmid et al. 2004). The complex consists mainly of poly-metamorphic siliciclastic
96 metasediments with minor amphibolites, eclogites and metapegmatites, as well as rare calc-
97 silicates and marbles.

98 The dominant tectono-metamorphic imprint in the Gneiss Unit of the Saualpe-Koralpe complex
99 occurred at eclogite facies conditions in the Cretaceous at around 90 Ma (Thöni 2006).
100 Maximum P-T conditions recorded by eclogites are 600 – 750ºC and 1.8 – 2.4 GPa (Gregurek et
101 al. 1997; Miller and Thöni 1997; Miller et al. 2005, 2007). Similar temperatures but lower
102 pressures are recorded by the metapelites (Gregurek et al. 1997; Tenczer and Stüwe 2003).

103 The Cretaceous tectono-metamorphic event was preceded by Permian low-pressure
104 metamorphism, evident from garnet cores (Thöni and Miller 2009), relict assemblages (Habler
105 and Thöni 2001; Tenczer et al. 2006) and radiometric dating (Thöni and Jagoutz 1992; Thöni et
106 al. 2008). Permian metamorphic conditions in the Saualpe-Koralpe complex have been estimated
107 at 600ºC/0.4 GPa (Habler and Thöni 2001) and 650ºC/0.6 – 0.65 GPa (Tenczer et al. 2006).
108 Widespread Al-rich pegmatites give undisturbed garnet Sm–Nd ages ranging from 285 to 225
109 Ma, indicating multiple melt injections (Thöni et al. 2008; Thöni and Miller 2009). Pegmatites

are interpreted as a product of local melting of siliciclastic (meta)sedimentary protoliths (Thöni and Miller 2000; Habler et al. 2007; Thöni et al. 2008) during long term thinning of the crust (Schuster and Stüwe 2008).

The Wirtbartl locality consists predominantly of Al-rich metapelites intercalated with peraluminous metapegmatites (Habler et al. 2007; Bestmann et al. 2008; Thöni et al. 2008). Garnet separates from different pegmatite bodies at the locality give Sm-Nd ages ranging from ca. 255 Ma (Habler et al. 2007) to ca. 230 Ma (Thöni et al. 2008).

Methods

Thin section preparation

Thin sections were polished mechanically and then chemo-mechanically (the latter using an alkaline colloidal silica suspension and a polyurethane plate) in order to produce a defect-free surface for EBSD analysis. Thin sections were carbon-coated to establish electrical conductivity. A single carbon thread at high vacuum ensured a thin coat for optimal EBSD measurement.

Field emission gun scanning electron microscope (FEG-SEM) and energy dispersive X-ray spectroscopy (EDX) analyses

Secondary electron (SE) and backscattered electron (BSE) images as well as EDX and EBSD analyses were collected on an FEI Quanta 3D FEG-SEM with a field emission gun source at the laboratory for scanning electron microscopy and focused ion beam applications of the Faculty of Geosciences, Geography and Astronomy at the University of Vienna (Austria). The microscope is equipped with an Apollo XV Silicon Drift Detector for EDX analysis. EDX data were collected using the TEAM 3.1 software at beam conditions of 15 kV and spot sizes of 4.5 - 5.5

(0.1 - 0.3 nA) in standard mode (30 - 50 μm aperture) or spot size 1.0 (4 nA) in analytic mode (1000 μm aperture).

EBSD analyses

Full crystallographic orientations of host garnet and rutile, ilmenite and corundum inclusions were determined by EBSD in two separate garnet grains. Measurements were carried out using the previously described FEI Quanta 3D FEG-SEM, equipped with an EDAX Digiview IV EBSD camera at an elevation angle of 5º. The OIM DC v6.2.1 EBSD analysis software was used for data acquisition. Beam conditions for all EBSD data were 15 kV accelerating voltage and 4.0 nA beam current with a 1000 μm SEM aperture and an incidence angle of 20º to the sample surface. The working distance was 14 mm and EBSD camera binning was 2 x 2, with Hough settings of 1º theta step size and a binned pattern size of 140 pixels. A 9 x 9 convolution mask with a maximum of 16 bands was used for indexing garnet. An 11 x 11 convolution mask with a maximum of 20 bands was used for indexing rutile, ilmenite and corundum. The same background was used throughout, but camera exposure time was increased when measuring corundum to compensate for lower signal intensity. The identity of inclusions was confirmed by EDX after measurement unless identification by EBSD pattern and inclusion habit was unequivocal. The Matlab^{TM} toolbox MTEX (Bachmann et al. 2010; Hielscher et al. 2010) was used for data processing and pole figure plotting.

Microstructural observations

Thin section description

The original (Permian) pegmatite microstructure of the samples has been affected by Cretaceous deformation and recrystallization (Bestmann et al. 2008; Griffiths et al., 2014). Polycrystalline quartz ribbons (grain size 40 μm – 1 mm), recrystallized feldspar (K-feldspar and albite, grain

size 40 – 150 μm) and acicular kyanite (grain size ~5 μm x 10 – 100 μm) define a mylonitic foliation. Magmatic almandine-spessartine garnet (grain size ~ 0.2 – 1 cm) and K-feldspar (perthitic, grain size up to ~ 1 cm) occur as porphyroclasts. Tourmaline, apatite and zircon are found as accessory minerals in the rock matrix. In less strained samples polycrystalline kyanite forms pseudomorphs completely replacing coarse-grained magmatic andalusite crystals.

In plane polarized transmitted light micrographs of thin sections garnet exhibits brownish-grey cores showing concentric and sector zoning (fig. 1), surrounded by clear pinkish rims with euhedral outer facets (fig. 2b+f). Rim garnet is intergrown with anhedral quartz (grain size 50 – 500 μm) and rare euhedral zircon (grain size ca. 100 μm). Both cores and rims are of Permian age (Thöni et al. 2008). The source of the dark coloration in cores is abundant submicrometer-sized inclusions (fig. 2), which are scarce or absent in the rims. Griffiths et al. (2014) document that these inclusions are 1 μm – 2 nm in diameter and that there are seven phases present: rutile, ilmenite, corundum, xenotime, zircon, apatite and qingheiite-Fe^{2+} (Hatert et al. 2010), a wyllieite group Fe-Mn phosphate (Moore and Ito 1979).

Inclusions define both concentric and sector zones in the garnet cores (fig. 1). Different zones are defined by variation in the abundances, grain sizes, habits or colors of the different inclusion phases. Transitions between concentric zones can be abrupt or gradual, and sometimes zoning is oscillatory (fig. 1a). Lateral transitions between sectors are always abrupt (e.g. fig. 1b). The outer boundaries of sector zones and all concentric zones are parallel to garnet crystal faces, primarily {112} and {110}.

Almost all inclusions that can be resolved optically are equant or slightly oblate, with no shape preferred orientation (fig. 2). The only exception is the intermittently developed outermost zone, which consists of elongate (0.2 – 0.5 x 10 – 100 μm) rutile needles with their long axes oriented

177 parallel to garnet <111> directions (not shown). Corundum inclusions are almost invisible in
178 transmitted light micrographs as they have a similar refractive index to garnet. SEM images (fig.
179 2d+h) reveal that they are tabular with a large aspect ratio (0.1 – 0.5 x 1 – 10 μm). Inclusions
180 large enough to be resolved in the SEM exhibit crystal facets; apatite and wyllieite group
181 phosphates have many facets, thus appearing rounded. Occasional multiphase inclusions can be
182 observed.

183 During Cretaceous eclogite facies metamorphism garnet underwent both crystal plastic and
184 brittle deformation. These processes locally promoted microstructural and compositional re-
185 equilibration of inclusions and garnet, resulting in two microstructures crosscutting the inclusion
186 zoning: recrystallization zones (Bestmann et al. 2008) and inclusion trails (Griffiths et al. 2014).
187 Both microstructures are surrounded by garnet where sub-micrometer inclusions are absent.

188 **EBSD measurement domains**

189 To study possible CORs between inclusions and garnet two domains were selected (fig. 2),
190 situated in the cores of separate but adjacent pegmatite garnets. Both have similar distributions of
191 inclusions, though inclusions in domain A are smaller and more abundant than inclusions in
192 domain B (fig. 2). SEM imaging and EDX measurements show that the most abundant phases in
193 both domains are rutile, corundum and wyllieite group phosphate. No ilmenite could be detected
194 in domain A, but ilmenite is present in domain B, where it is rarer and smaller than rutile and
195 corundum. These differences reflect the fact that the domains are at different positions in the
196 zoning succession. Domains were selected to avoid the areas of optically visible re-equilibration
197 associated with inclusion trails and recrystallization zones.

198 **Crystallographic orientation data**

EBSD point analyses determined the crystallographic orientation of host garnet, corundum, rutile and ilmenite. Indexing of xenotime and zircon EBSD patterns generated multiple orientation solutions for single inclusion crystals. No reference pattern was available for wyllieite group phosphates and both wyllieite and apatite inclusions were sensitive to beam damage. In light of these methodological obstacles and their relative scarcity in the selected domains, EBSD data was not collected for zircon or any phosphate phases.

Representativeness and precision of the EBSD single point dataset

Emphasis was placed on collecting a large number of measurements for each inclusion phase; the total number of inclusions analyzed does not reflect the relative abundance of each phase. However, the relative frequency of different CORs within each phase is expected to be representative for the grainsizes that could be measured (minimum ca. 400 nm parallel to the long axis of the EBSD interaction volume) because the only selection criterion was sufficient pattern quality for indexing. All rutile and corundum CORs with N>3 inclusions were found in both garnets. Some CORs are up 2.5 times more frequent in one garnet domain compared to the other (table S1).

A rough estimate of the precision of orientation determination was obtained by calculating the average misorientation angle between five garnet orientations measured on the same crystal and the mean orientation of the five measurements. The measurements differed from the mean orientation by an average of 0.7º, and a similar value was obtained for three repeat measurements on a second garnet crystal. The estimated precision in misorientation angle between two independent measurements is thus 1.4º.

Pole figure plot construction

All pole figures were plotted with antipodal symmetry. To enable comparison between garnets all inclusion orientations were plotted relative to a fixed host garnet orientation (x ∥ $[100]_{garnet}$ and z ∥ $[001]_{garnet}$). No garnet direction was strongly preferred over any of its symmetrical equivalents for any COR in either garnet. This allowed the combination of data from separate garnets and meant that a partial symmetrization of the dataset could be carried out to make CORs clearer in pole figures without introducing spurious symmetries. Four copies of the dataset were overlapped, each rotated by 90º around garnet [001] relative to each other, forcing the dataset to conform to the fourfold symmetry of the garnet [001] axis. A single quadrant of the resulting pole figure contains the orientation relationship information of the whole dataset, combining inclusions that have CORs with symmetrically equivalent garnet axes. Symmetrized plots are indicated in figure captions.

Rutile crystallographic orientations

The crystallographic orientation of rutile inclusions relative to the host garnet reflects the symmetry of the garnet structure (fig. 3). Rutile inclusions were divided into groups based on the alignment of their <001> directions (*c*-axes) with different directions in garnet (fig. 3). Groups were divided into subgroups according to the relationships of other rutile directions with garnet. The suggested CORs of undivided rutile inclusion groups and the most abundant subgroups are listed in table 1.

Group R1 (fig. 4a). This group comprises rutile inclusions with their *c*-axes parallel to garnet <110> with ≤ 5º misorientation, corresponding to maxima in the *c*-axis ODF plot (fig. 3). Only 30% of inclusions in group R1 have *c*-axes that lie within 1.4º of garnet <110>. The distribution of misorientation angles between rutile *c*-axes and garnet <110> is shown in figure 4b. Subgroup R1a comprises the majority of group R1. One of the two symmetrically equivalent rutile *a*-axes

is parallel to a garnet <111> direction and the second is parallel to a garnet <112> direction (both with up to 5º misorientation, fig. 4a). In the small subgroup R1b (fig. S1a), *a*-axes appear to follow one set of higher-order symmetrically equivalent directions in garnet. Given the 5º orientation spread it is difficult to specify these, but the garnet <144> and <118> directions are a good approximation.

Group R2 (fig. S1b). This group comprises the four rutile inclusions with a *c*-axis parallel to garnet <111> with ≤ 5º misorientation. The mean misorientation angle between rutile *c*-axes and garnet <111> is 0.7º. In subgroup R2a one of the rutile *a*-axes is parallel to a garnet <110> direction and the second is parallel to a garnet <112> direction, with no significant misorientation. The *a*-axes of one inclusion lie within a garnet {111} plane but not parallel to any low-indexed garnet directions, it is assigned to subgroup R2b.

Group R3 (fig. 5). This group comprises rutile inclusions with a *c*-axis lying in a cone inclined to the garnet <111> directions. The angle which the rutile *c*-axis makes to the nearest garnet <111> direction will be referred to as the 'inclination angle'. This relationship was previously described by Proyer et al. (2013), who recorded inclination angles from 26º - 29º (mean 27.6º). Group R3 encompasses all rutile inclusions with inclination angles of 26º - 31º (mean 28.1º). Rutile *c*-axes are not evenly distributed around garnet <111>. Six maxima form three pairs flanking each garnet <110> direction, conforming to the threefold symmetry axis along garnet <111> (fig. 3). These diffuse maxima coincide with garnet <135> directions. Three weaker maxima occur between these pairs, centered on garnet <113> directions. Group R3 was divided into 3 subgroups.

Subgroup R3a (fig. 5a), the largest, corresponds to the orientation relationship seen by Proyer et al. One rutile *a*-axis lies in or near to the {111} plane perpendicular to the <111> direction

around which the rutile *c*-axis cone lies (fig. 5ai). The second *a*-axis is forced by symmetry to lie on a small circle at ± the inclination angle from the {111} plane, i.e. rutile orientations are tilted around the *a*-axis in the garnet {111} plane by the inclination angle. The *a*-axes in garnet {111} planes never occur within ca. 10º of a garnet <110> direction but otherwise no direction within the plane is avoided. The inclined *a*-axes show a preference for garnet <112> directions. The low-indexed rutile direction aligned closest to garnet <111> is one of the rutile <103> directions (fig. 5aii). 56% of inclusions in subgroup R3a have a rutile <103> direction within 1.4º of garnet <111>. No low-indexed garnet directions coincide with other rutile <103> directions, which lie in two cones ca. 38º and 55º inclined to garnet <111>. One small circle of {101} poles is inclined only 5º to garnet <111> and a second small circle lies at the *c*-axis inclination angle from the {111} plane, coinciding with the rutile *a*-axis small circle (fig. S2a). Rutile {101} poles show no preference for a garnet direction. All other orientation relationships described by Proyer et al. follow by symmetry from the relationships described here.

Subgroup R3b (fig. 5b) comprises group R3 inclusions where one rutile {101} plane pole is parallel to a garnet <110> direction (fig. 5bii). The *c*-axes of these inclusions cluster near to garnet <113> directions (within the previously defined cone around garnet <111>), but do not follow the <113> directions strictly. In contrast to subgroup R3a, rutile *a*-axes are not perpendicular to the garnet <111> direction around which the *c*-axis cone is located (fig. 5bi). One *a*-axis appears concentrated near to garnet <112> directions that do not lie perpendicular to garnet <111> and some rutile <103> directions seem to cluster near garnet <135> directions (fig. S2b), but there are not enough data to be confident about these potential relationships.

Subgroup R3c (fig. S2c) comprises the nine group R3 inclusions with *c*-axes that lie within the cone around a garnet <111> direction, but for which no other relationships with garnet could be

found. Rutile *c*-axes cluster near to garnet <135> directions (though this was not the criteria used to define the subgroup). It is possible that there are other alignments between garnet and rutile directions but sampling statistics for this subgroup are too poor to make them obvious.

Group R1* (fig. 4c). This group represents a broad spread of *c*-axis orientations. Of all inclusions not belonging to groups R1, R2 or R3, over 80% are oriented with their *c*-axes between 5º and 22º from a garnet <110> direction (fig. 3), and are assigned to this group. The distribution of misorientation angles between rutile *c*-axes and garnet <110> is shown in figure 4b. Inclusions satisfying the *c*-axis criterion for group R3 have been excluded from group R1*. The orientation relationships of rutile directions other than <001> with garnet are as diffuse as the *c*-axis distribution. One of the two rutile *a*-axes tends to cluster parallel or near to a garnet <111> direction. However, almost no rutile *a*-axes are found aligned with a garnet <112> direction, and the remaining *a*-axes define a broad girdle around the {110} plane.

Group RX (fig S3a). This group comprises rutile inclusions where no orientation relationship with the garnet could be observed.

Corundum crystallographic orientations

The crystallographic orientation of corundum inclusions relative to the host garnet also reflects the symmetry of the garnet. Multiple groups can be identified based on the alignment of corundum <0001> directions (*c*-axes) with different garnet directions. Groups were divided into subgroups according to the relationships of other corundum directions with garnet. The CORs of undivided corundum inclusion groups and the most abundant subgroups are listed in table 2. The tabular habit of corundum inclusions is defined by their crystallography, with tablets parallel to

311 corundum {0001} planes. All corundum CORs therefore imply corresponding shape-preferred
312 orientation relationships.

313 **Group C1 (fig. 6a).** This group comprises corundum inclusions with a *c*-axis parallel to the
314 garnet <112> direction with ≤ 5º misorientation. 78% of these inclusions have a *c*-axis within
315 1.4º of garnet <112>. Most inclusions belong to subgroup C1a. One corundum *a*-axis (parallel to
316 the poles of corundum {11-20} planes) is aligned with a garnet <111> direction (fig 6ai). By
317 symmetry the other two *a*-axes align close to garnet <113> directions. Correspondingly,
318 corundum {10-10} poles are aligned at 30º to the *a*-axes, one {10-10} pole is fixed parallel to
319 garnet <110> and the other two lie near to garnet <135> directions (fig 6aii). The small subgroup
320 C1b is identical to C1a except that inclusions are rotated 30º around their *c*-axes. Two inclusions
321 have *a*-axes in garnet {112} planes that are not parallel to any of the important garnet directions
322 seen in the other subgroups, these are assigned to subgroup C1c.

323 **Group C2 (fig. 6b).** This group comprises corundum inclusions with a *c*-axis parallel to the
324 garnet <111> direction with ≤ 5º misorientation. 84% of the group has a *c*-axis within 1.4º of
325 garnet <111>. Almost all inclusions are assigned to subgroup C2a, where all corundum *a*-axes
326 (fig 6bi) are parallel to garnet <112> directions and all {10-10} poles (fig. 6bii) are parallel to
327 garnet <110> directions. Subgroup C2b comprises the 3 inclusions where corundum *a*-axes are
328 merely located within a garnet {111} plane and are not systematically parallel to a low-indexed
329 garnet direction.

330 **Group C3 (fig. S4).** This group comprises the small number of corundum inclusions with a *c*-
331 axis parallel to the garnet <100> direction with ≤ 5º misorientation. The mean misorientation
332 angle between group C3 corundum *c*-axes and garnet <100> is 1.47º. One corundum *a*-axis is
333 always parallel to a garnet <110> direction, as by symmetry is one {10-10} pole.

Group C4 (fig. 6c). This group comprises corundum inclusions without a *c*-axis within ≤ 5º misorientation angle of either garnet <111> or <112> directions, but with one *a*-axis (fig. 6ci) parallel to a garnet <111> direction (with ≤ 5º misorientation). 38% of inclusions in the group have one *a*-axis within 1.4º of garnet <111>. The corundum *c*-axes lie in {111} garnet planes, as does one of the {10-10} poles (fig. 6cii). This group has not been divided into subgroups as there are no symmetrically repeated concentrations of corundum {10-10} poles, *c*- or *a*-axes parallel to low indexed garnet directions. Nonetheless group C4 corundum *c*-axes do not appear randomly distributed around one *a*-axis, but this may be an artifact of the small number of grains comprising this group.

Group CX (fig S3b). This group comprises corundum inclusions where no orientation relationship with the garnet could be observed.

Ilmenite crystallographic orientations

The crystallographic orientation of ilmenite inclusions relative to the host garnet also reflects garnet symmetry. Groups were defined based on the alignment of ilmenite <0001> directions (*c*-axes) with different garnet directions and divided into subgroups using the relationships of other ilmenite directions with garnet. The CORs of undivided ilmenite inclusion groups and the most abundant subgroups are listed in table 3.

Group I1 (fig. 7a). This group comprises ilmenite inclusions with a *c*-axis parallel to the garnet <112> direction with ≤ 5º misorientation. 86% of the group has their *c*-axis within 1.4º of garnet <112>. In the largest subgroup, I1a, one ilmenite *a*-axis (equivalent to one ilmenite {11-20} plane pole) is aligned with a garnet <111> direction (fig. 7ai). The other *a*-axes align close to garnet <113> directions. One ilmenite {10-10} pole is fixed parallel to garnet <110> and the

other two lie near to garnet <135> directions (fig. 7aii). The small subgroup I1b is identical to I1a except that inclusions are rotated 30º around their *c*-axes. Six inclusions have *a*-axes in garnet {112} planes that are not parallel to any of the important garnet directions seen in the other subgroups, these are assigned to subgroup I1c.

Group I2 (fig. 7b). This group comprises ilmenite inclusions with a *c*-axis parallel to the garnet <111> direction with ≤ 5º misorientation. 95% of the group has a *c*-axis within 1.4º of garnet <111>. All but one inclusion are assigned to subgroup I2a, where all ilmenite *a*-axes are parallel to garnet <112> directions (fig. 7bi) and all {10-10} poles are parallel to garnet <110> directions (fig. 7bii). A single inclusion has *a*-axes located within a garnet {111} plane but not parallel to a low-indexed garnet direction, assigned to subgroup I2b.

Group I3 (fig. 7c). This group comprises ilmenite inclusions without a *c*-axis within ≤ 5º misorientation angle of either garnet <111> or <112> directions, but with one *a*-axis (fig. 7ci) parallel to a garnet <111> direction (with ≤ 5º misorientation). 65% of inclusions in the group have one *a*-axis within 1.4º of garnet <111>. The ilmenite *c*-axes lie in {111} garnet planes, as does one of the {10-10} poles (fig. 7cii). This group has not been divided into subgroups as there are no symmetrically repeated concentrations of ilmenite {10-10} poles, *c*- or *a*-axes parallel to low indexed garnet directions.

Group IX (fig S3c). This group comprises ilmenite inclusions where no orientation relationship with the garnet could be observed.

Discussion

89% of the 530 inclusions analyzed by EBSD have crystallographic orientations that can be related to the crystal symmetry of the host garnet. Each of the three inclusion phases examined

can be divided among at least three different groups (most with several subgroups) on the basis of orientation relationships between host and inclusion crystallographic directions. The Wirtbartl host–inclusion system displays exceptional variety in the number and type of CORs present.

The origin of the Wirtbartl inclusions is not discussed here. This would require a full picture of the CORs present in host–inclusion systems with different known inclusion origins, something this paper suggests is not yet available.

Types of COR

Nomenclature is required to discuss the diverse characteristics of the observed CORs. The proposed terminology for COR types does not carry any genetic implications. In this discussion, the term ‘specific COR’ refers to a crystallographic orientation relationship where the orientations of inclusion and host are fixed with respect to one another, with zero degrees of freedom. It makes no reference to the coherency of the two lattices or the interface geometry and structure.

About half the COR groups described do not show a specific COR to the host garnet. Nonetheless, the distribution of inclusion crystallographic orientations in these groups reflects the symmetry of the garnet (e.g. fig. 3). The term 'statistical COR' is introduced to describe the relationships between host and inclusion directions that are not specific but non-random. A statistical COR is defined by a population of inclusions. The crystallographic orientations of individual inclusions with a particular statistical COR have one or more degrees of freedom relative to the crystallographic orientation of the host, although there may be limits to the range of misorientation angles over which this freedom exists. EBSD measurement of increasing numbers of inclusions with the same statistical COR reveals an orientation distribution that

400 increasingly accurately approximates conformity to the centrosymmetric point group symmetry
401 of the host crystal.

402 The inclusion orientation distributions of statistical CORs display two end member
403 characteristics. A statistical COR usually exhibits a mixture of both. In some groups, one
404 inclusion crystallographic direction is fixed to the host and the others are free to assume any
405 direction rotated around this common axis, i.e. inclusion crystallographic orientations have one
406 degree of freedom (subgroup R3a, fig. 5a; group C4, fig. 6c; subgroup I1c, fig. 7a; group I3, fig.
407 7c; Proyer et al. 2013; Xu et al. 2015). This characteristic of a statistical COR will be referred to
408 as 'rotation'. 'Rotational' statistical CORs are those where rotation is the strongest element of the
409 inclusion orientation distribution. In most examples the single degree of freedom is limited, so
410 that not every orientation distributed around a certain direction is equally favored (e.g. subgroup
411 R3a, fig. 5a; Xu et al. 2015).

412 Other groups show inclusion crystallographic directions concentrated within a certain
413 misorientation angle of particular host crystallographic directions, but not fixed exactly parallel
414 to them (groups R1 and R1*, fig. 4; subgroups R3b and R3c, figs. 5b & S2c). Such groups allow
415 two degrees of freedom between host and inclusion crystallographic orientations, but only within
416 strict limits. This characteristic of a statistical COR will be referred to as 'dispersion'.
417 'Dispersional' statistical CORs are those where dispersion is the strongest element of the
418 inclusion orientation distribution; if one crystallographic direction were less dispersed then the
419 statistical COR would be rotational in character. Rotational CORs often show subordinate
420 dispersion (all rotational CORs listed in the previous paragraph; Xu et al. 2015).

Due to the complexity inherent in precisely determining the error of lattice orientations derived from SEM-EBSD analyses (e.g. Ram et al. 2015), a generalized criterion to differentiate specific CORs from statistical CORs at very small dispersions is beyond the scope of this paper. In the Wirtbartl dataset the two predominantly dispersional statistical CORs (groups R1 and R1*) can nonetheless be reliably classified because the observed dispersion greatly exceeds the expected angular error of Hough-transform-based EBSD (fig. 4).

An indication of the amount of dispersion of an axis relationship can be obtained by calculating the fraction of inclusions in a group that fulfill the chosen relationship with a misorientation angle below a set value. This has been carried out for the Wirtbartl dataset for groups containing > 10 inclusions, using an angle of 1.4°, twice the approximate angular precision of the garnet orientation measurements. For axis relationships that are considered specific (groups C1, C2, I1 and I2) > 75% of all inclusions have misorientation angles of less than 1.4°, whereas in groups with minor or major dispersional character, < 65% of all inclusions fulfill this criterion. It is not considered useful to subdivide groups depending on whether each inclusion exceeds the angular cutoff or not as there is no evidence that there would be a physical or genetic distinction between the resulting subgroups.

Table S2 summarizes how the CORs of all (sub)groups listed in tables 1 – 3 have been classified, according to the criteria discussed above.

Why use the statistical COR concept?

General considerations. Currently, studies of host–inclusion systems often look for evidence of specific CORs, rather than fully describing the distribution of inclusion orientations present. The statistical COR concept encourages a less binary approach, in accordance with the wide variety

443 of CORs observed in this and other studies (Proyer et al. 2013; Xu et al. 2015) that are not
444 specific. It also highlights the need for larger numbers of orientation measurements when
445 studying CORs.

446 Once inclusion directions are separated by less than twice the angular error of the EBSD
447 measurement from each other, the distribution of directions is indistinguishable from continuous.
448 Below this limit (e.g. subgroup R3a, fig. 5a; group C4, fig. 6c) it is inappropriate to represent the
449 distribution of orientations as a large number of different specific CORs.

450 **Illustrative case study: re-examination of Hwang et al. (2007, 2015).** Re-examining some
451 previous results provides an example of how the concept of statistical CORs can capture details
452 of host–inclusion crystallographic relationships that are otherwise obscured.

453 Hwang et al. (2015) present TEM data on the interfaces and CORs of rutile needles in garnet
454 from multiple sources: detrital Idaho 'star garnet' most likely originally from polymetamorphic
455 amphibolite facies metapelitic schist (West et al. 2005; Lang et al. 2014) and garnets from two
456 ultra-high-pressure (UHP) localities: an eclogite from the Sulu UHP terrane in China and a
457 microdiamond-bearing rock from the Erzgebirge, Germany. The Idaho garnets are the main
458 focus of the study, whereas the UHP sample measurements are an expansion of a smaller dataset
459 presented in Hwang et al. (2007).

460 Hwang et al. (2015) define seven major garnet–rutile CORs, all exclusively specific. Their COR-
461 1, COR-5 and COR-6 are not found in the Wirtbartl garnets, and their COR-4 (corresponding to
462 subgroup R2a) is present but rare in both datasets. Comparison of the three remaining Hwang et
463 al. CORs with the rotational statistical COR of group R3a provides evidence of statistical CORs
464 in the older datasets. Rutile inclusions with crystallographic orientations corresponding to

Hwang et al.'s COR-2 & COR-2' ($[103]_{Rt} \parallel [111]_{Grt}$ & $(0\pm10)_{Rt} \parallel (4\text{-}3\text{-}1)_{Grt}$, COR-2 and COR-2' are indistinguishable by EBSD) are common in the Wirtbartl garnets. The same is true for their COR-3 ($[103]_{Rt} \parallel [111]_{Grt}$ & $(010)_{Rt} \parallel (2\text{-}1\text{-}1)_{Grt}$). For the Wirtbartl dataset it is immediately obvious that the <010> directions (*a*-axes) of inclusions with $<103>_{Rt} \parallel <111>_{Grt}$ are not *limited* to being parallel to either $<4\text{-}3\text{-}1>_{Grt}$ or $<2\text{-}1\text{-}1>_{Grt}$. Rutile *a*-axes can lie anywhere in the {111} plane, with the exception of positions within ca. 10º of a garnet <110> direction (group R3a, fig. 5ai).

Hwang et al. (2015) document rutile inclusions with small misorientations from their specific CORs, describing these as 'angular misfits of xº' or 'xº off' from a particular axis relationship. Multiple angular misfits are explicitly described in the Hwang et al. (2015) measurements from the Sulu UHP garnet sample. For inclusions close to COR-2/2', the reported range of angular misfits is greater (0 - 6º) for rutile *a*-axes than for the perpendicular rutile <103> directions (0 - 2º), i.e. these inclusions are misoriented around a rotation axis close to garnet <111> from the ideal COR. Inclusions close to COR-3 reportedly do not show any angular misfit for rutile <103> directions but show angular misfits of 0 - 3º for their *a*-axes, corresponding to a pure rotation around garnet <111>. Taking the extremes of both ranges implies that only 7º of the 16.1º angle between neighboring $<2\text{-}1\text{-}1>_{Grt}$ and $<4\text{-}3\text{-}1>_{Grt}$ directions remains unoccupied by rutile *a*-axes in the reported dataset. Given that the Sulu garnet dataset presented in Hwang et al. (2015) consists of only 19 rutile inclusion orientations, 17 with COR-2/2' or COR-3 orientations, there is a strong possibility that further measurements might reveal a continuous distribution of rutile *a*-axes in the garnet {111} plane, similar to that of the Wirtbartl garnets. This possibility is supported by the 5 Sulu rutile needles plotted by Hwang et al. (2007) that have *c*-axes in a cone around a garnet <111> direction and *a*-axes in a garnet {111} plane (implying one $<103>_{Rt}$ is

488 approximately parallel to <111>$_{Grt}$). None of these inclusions have *a*-axes that coincide with <2-
489 1-1>$_{Grt}$, <4-3-1>$_{Grt}$, or <1-10>$_{Grt}$, and one particular *a*-axis (a_6) is approximately halfway
490 between a <2-1-1>$_{Grt}$ and a <4-3-1>$_{Grt}$ direction (fig. 8).

491 Hwang et al. (2015) do not explicitly give the percentage of inclusions with angular misfits for
492 every sample, but in contrast to the Sulu garnets, the Idaho star garnets appear to mostly show
493 inclusions without angular misfits. Of 58 inclusions measured in one sample (a 6-ray star garnet
494 showing 6 different CORs), only one is called out as having any angular misfit. The distribution
495 of rutile inclusion crystallographic orientations in the 6-ray Idaho star garnet is therefore best
496 described by multiple specific CORs, even using the stricter definition preferred in this paper.

497 The existence of a range of rutile inclusion crystallographic orientations arrayed around a
498 common host garnet axis (a rotational statistical COR) is a reproducible and important
499 characteristic of the Sulu garnet samples that is obscured by describing the distribution as a
500 number of specific CORs with 'angular misfit[s]'. The Sulu orientation distribution appears
501 distinguishable from that in the Idaho star garnets, where the large majority of rutile inclusions
502 *do* have completely specific CORs (assuming that all instances of angular misfit have been
503 explicitly reported). This fact may be of petrological significance, but previous terminology has
504 not allowed for such distinctions to be unambiguously stated.

505 A final judgment on the continuity of rutile *a*-axis distributions in garnet {111} planes in the
506 Sulu samples must await measurement of a larger number of rutile crystallographic orientations.
507 However, even if further measurements were to confirm the current angular misfit ranges for
508 COR-2/2' and COR-3 as the maximum variation present in the Sulu sample, the description of
509 these CORs as specific would remain misleading. If the current ranges describe the true

maximum variation, the individual groupings COR-2, COR-2' and COR-3 can be retained. However, they should then be described as rotational statistical CORs to denote the nature of the angular variation within each population. Should further measurements instead reveal a continuous distribution, a single rotational statistical COR would most correctly describe the systematic distribution of inclusion orientations with $<103>_{Rt} \parallel <111>_{Grt}$.

The uncertainty about the rotational statistical COR(s) in the Sulu sample stems directly from the limited number of rutile crystallographic orientations reported so far. However, no matter how large the dataset, small groups of inclusions from which the full particulars of a COR cannot be reliably determined will almost always be found (e.g. subgroup R2b, fig. S1b; subgroups C1c & C2b, fig. 6a+b; subgroups I1c & I2b, fig. 7a+b). The most general description for a group of inclusions with one axis fixed relative to the host is a single rotational statistical COR, and in the absence of sufficient measurements to reveal greater detail, this is the recommended description. The inclusions in the Sulu sample with $<103>_{Rt} \parallel <111>_{Grt}$ should be described as belonging to a single rotational statistical COR until further data becomes available.

Comparison of Wirtbartl COR data with literature CORs

Existing literature data on CORs between garnet and corundum are restricted to intergrowths between corundum and yttrium aluminium garnet. Sugiyama et al. (2009) found the same COR as the commonest COR in this study (subgroup C1a, fig. 6a), $<0001>_{corundum\ (Crn)} \parallel <112>_{garnet\ (Grt)}$ & $\{11\text{-}20\}_{Crn} \parallel \{111\}_{Grt}$. Frazer et al. (2001) detected the COR $<0001>_{Crn} \parallel <112>_{Grt}$ & $\{10\text{-}10\}_{Crn} \parallel \{111\}_{Grt}$, observed only rarely in this study (subgroup C1b, fig. 6a). No literature could be located on CORs between garnet and ilmenite. However, in the Wirtbartl data there is great similarity between the CORs of the two different trigonal phases with garnet. All COR groups

identified for ilmenite are also shown by corundum. This similarity extends to broader similarity with literature data for CORs between trigonal and cubic crystals. The hematite-magnetite system shows condition-dependent variation between the axis relationships $<0001>_{\text{hematite (Hem)}}$ $\|<111>_{\text{magnetite (Mag)}}$ and $<0001>_{\text{Hem}} \|<112>_{\text{Mag}}$ (Bursill & Withers 1979), and for the axis relationship $<0001>_{\text{Hem}} \|<111>_{\text{Mag}}$ both the relationships $\{10\text{-}10\}_{\text{Hem}} \| \{110\}_{\text{Mag}}$ (e.g. Bursill & Withers 1979) and the relationship $\{11\text{-}20\}_{\text{Hem}} \| \{110\}_{\text{Mag}}$ (Amouric et al. 1986) have been found to exist. The range of possible CORs between two phases can seemingly be estimated knowing only their respective crystal systems, suggesting that the role of conserved symmetry elements in controlling CORs is large. Despite the existence of a range of *possible* CORs, the simultaneous occurrence of so many of these in one system does appear to be an unusual feature of the Wirtbartl garnets.

At present, the host–inclusion system for which the most varied COR data is available is the garnet–rutile system. Despite uncertainties concerning inclusion formation mechanisms and the conditions and timing of COR formation, an overview of reported garnet–rutile CORs gives an indication of distinguishable characteristic features and possible trends. Rutile–garnet CORs have been described from five garnet localities: detrital ‘star garnets’ most likely from polymetamorphic amphibolite facies metapelitic schists (West et al. 2005; Lang et al. 2014) in Idaho (Guinel & Norton 2006; Hwang et al. 2015); garnets from eclogite layers in an ultramafic complex in the Sulu UHP terrane, China (Hwang et. al 2007, 2015); garnets containing microdiamonds from the Erzgebirge, Germany (Hwang et. al 2007, 2015); granulite facies garnet rims on UHP garnets from a kyanite-garnet mica-schist in the Kimi complex, Rhodope Massif, Greece (Proyer et al. 2013); and low pressure pegmatite garnets from the locality Wirtbartl, Koralpe, Eastern alps (this study). The Erzgebirge garnet–rutile CORs are not described in

555 sufficient detail to judge whether they are statistical or specific, so are not included in the
556 discussion below.

557 The axis relationship $<103>_{\text{rutile (Rt)}} \parallel <111>_{\text{Grt}}$ is found at every locality, but there are
558 differences in the arrangement of rutile *a*-axes in {111} garnet planes between the localities. In
559 Idaho star garnet there are reportedly multiple specific CORs involving $<103>_{\text{Rt}} \parallel <111>_{\text{Grt}}$,
560 with COR-2/2' rutile *a*-axes parallel to $<4\text{-}3\text{-}1>_{\text{Grt}}$ (the sole COR present in one garnet analyzed),
561 COR-3 rutile *a*-axes parallel to $<2\text{-}1\text{-}1>_{\text{Grt}}$ and COR-1 rutile *a*-axes parallel to $<1\text{-}10>_{\text{Grt}}$
562 (Hwang et al. 2015). This last axis relationship is found *only* in the Idaho garnets. In contrast,
563 there is a single rotational statistical COR around $<103>_{\text{Rt}} \parallel <111>_{\text{Grt}}$ reported for rutile needles
564 in garnet from the Rhodope and from equant rutile inclusions in this study (subgroup R3a), with
565 rutile *a*-axes found at all points in the garnet {111} plane apart from close to garnet <1-10>
566 directions (this study fig. 5; Proyer et al. 2013). The dataset is of limited size, but the same
567 rotational statistical COR also seems to be shared by inclusions with $<103>_{\text{Rt}} \parallel <111>_{\text{Grt}}$ in the
568 Sulu garnets (Hwang et al. 2007, 2015). Rutile inclusions with *c*-axes concentrated on
569 dispersional statistical CORs around garnet <110> directions comprise ca. 50% of the 250
570 inclusions measured in the Wirtbartl samples, but are not observed at any of the other localities.
571 The COR $<001>_{\text{Rt}} \parallel <111>_{\text{Grt}}$ & $<010>_{\text{Rt}} \parallel <1\text{-}10>_{\text{Grt}}$ is found in the Idaho garnets (where it is
572 designated COR-4), the Rhodope garnets, and in this study (corresponding to subgroup R2a), but
573 is very rare in all cases. CORs involving $<001>_{\text{Rt}} \parallel <001>_{\text{Grt}}$ are found occasionally in the Sulu
574 garnets and commonly in certain Idaho garnets (11 of 58 inclusions measured in one garnet have
575 Hwang et al.'s COR-5; $[001]_{\text{Rt}} \parallel [001]_{\text{Grt}}$ & $(010)_{\text{Rt}} \parallel (1\text{-}10)_{\text{Grt}}$), such CORs are not found
576 elsewhere.

577 The data available show that multiple rutile–garnet CORs are common in single localities and
578 that similarities exist between CORs over a wide range of conditions. This suggests strong
579 favorability of certain axis relationships. Whether this is a consequence of energetically
580 favorable lattice-scale interactions or common inclusion formation processes (or both) is
581 unknown. Alongside broad similarities there are variations between (and in the case of the Idaho
582 garnets even within) localities. The two localities with at least one unique COR (Idaho and
583 Wirtbartl) are the two with very different implied conditions of formation to the UHP and
584 granulite garnets. The Wirtbartl data are the only results from equant rutile inclusions rather than
585 needles, this may also contribute to the observed differences. The literature comparison
586 corroborates the impression given by the corundum and ilmenite data that the Wirtbartl garnets
587 exhibit an unusually high number of different CORs for a single locality.

588 **Lattice-based explanations for the Wirtbartl CORs?**

589 A lattice matching (or coherency) model (e.g. Howe 1997; Balluffi et al. 2005) predicts
590 orientation relationships well for phases with similar crystal symmetries and structures.
591 However, the Wirtbartl inclusions have heterophase interfaces, separating different crystal
592 systems and oxygen sublattices. Calculated lattice strain was used to compare parallel sets of
593 planes from observed CORs to examine whether lattice matching can explain their favorability.
594 Physically, lattice mismatches may be accommodated by elastic strain, misfit dislocations or an
595 incoherent interface (Howe 1997).

596 Tables 1 – 3 list the sets of parallel garnet and inclusion plane poles or directions that define the
597 largest COR (sub)groups. Whenever directions are listed, the indices of the direction are
598 identical to the pole of a plane with equivalent indices. A pair of parallel related planes was

599 designated *(hkl)* for garnet and *(mno)* for inclusions. The d-spacings of sets of garnet planes
600 (*HKL*) = *x**(*hkl)* and inclusion planes *(MNO)* = *y**(*mno)* were used to calculate lattice strains.
601 The variables *x* and *y* are positive scalar integers. Calculated lattice strains depend on the size of
602 *x* and *y*, referred to here as the 'order' of the *(HKL)* and *(MNO)* planes. In this work low-order
603 planes are preferred, as these are more likely to correspond to layers of atoms in the crystal. The
604 lowest-order pair of planes that could achieve a strain of between -0.04 and +0.04 (an arbitrary
605 target) was determined for each planar relationship in tables 1 – 3. Lattice strain was calculated
606 as $\frac{d_{(MNO)\ inclusion} - d_{(HKL)\ garnet}}{d_{(HKL)\ garnet}}$, where $d_{(MNO)}$ represents the d-spacing of *(MNO)* planes. If only
607 very high order planes met the target, the strain for a 1:*x* or *y*:1 ratio of orders was calculated for
608 comparison purposes, with *x* (or *y*) chosen to minimize the lattice strain. The results are given in
609 tables 4 – 6. Bolded relationships are those where the target lattice strain can be achieved using
610 orders ≤ 3, assumed to indicate the best matches.

611 Using $d_{\text{inclusion}}$ as the denominator instead has negligible effect for small lattice strains. For lattice
612 strains > 0.1 there is a difference of ≥ 20%. The effect of pressure has been neglected as the
613 pegmatites formed at no more than 0.3 GPa (Habler et al. 2007). Calculations used lattice
614 constants measured at room pressure and at room temperature and 600ºC (table S3). Room
615 temperature values are discussed here; lattice strains calculated using cell parameters at 600ºC
616 differ by ≤ 0.01 (tables S4-S6).

617 The lattice-matching hypothesis posits that common, specific CORs should have multiple good
618 d-spacing fits between inclusion and host, with rotational CORs occurring where one set of
619 planes has a much better fit than the planes oriented at a high angle to them.

Rutile CORs (table 4). A good low-indexed fit was not found for the relationship $\{001\}_{\text{rutile (Rt)}} \parallel \{110\}_{\text{garnet (Grt)}}$, which fits with the observation that although rutile *c*-axes are concentrated near garnet <110> directions there is significant dispersion (subgroup R1a, group R1*, fig. 4). The calculated fits for the rutile {100} plane relationships of subgroup R1a are good, including a 1:1 correspondence between $\{100\}_{\text{Rt}}$ and $\{112\}_{\text{Grt}}$ with only 3% misfit. Despite this, rutile *a*-axes show similar amounts of dispersion to the *c*-axes for subgroup R1a, and the relationship $\{100\}_{\text{Rt}} \parallel \{112\}_{\text{Grt}}$ is absent in group R1*.

Only one of the three sets of planes examined for each COR in subgroups R2a and R3b shows a good calculated fit with garnet. Despite this, neither COR shows a rotational component, although both are rare as would be expected for poorly fitting CORs.

In subgroup R3a a single rutile <103> direction (pole to a {405} rutile plane) is aligned (sub)parallel to garnet <111>. There is a poor fit between rutile {405} planes and garnet, the most plausible relationship being $\{405\}_{\text{Rt}} \parallel \{12\ 12\ 12\}_{\text{Grt}}$ (lattice strain 0.06). However, the <103> rutile vector is almost exactly equal to half the <111> garnet vector (misfit strain only 0.004). Despite poor agreement between {405} rutile planes and garnet plane families parallel to {111}, the similarity between crystal vector lengths somehow favors this axial orientation relationship. Rutile inclusions can rotate around the fixed <103> direction despite the good fits exhibited by rutile {100} planes.

Corundum CORs (table 5). Despite only one set of planes having a low-indexed, low lattice strain fit with garnet, subgroup C1a is specific and also the commonest corundum COR. Subgroup C2a is slightly less common than subgroup C1a, despite being the *only* COR for which three perpendicular sets of well-fitting planar relationships are calculated. No good low index fit exists for the only fixed set of planes of the group C4 rotational statistical COR. No rotational

643 statistical COR is developed around the much better fitting pair of $\{10\text{-}10\}_{\text{corundum}} \| \{220\}_{\text{Grt}}$
644 planes (lattice strain -0.01).

645 **Ilmenite CORs (table 6).** Ilmenite subgroups I1a and I2a share the same COR as corundum
646 subgroups C1a and C2a. But whereas in subgroup C1a the {10-10} planes achieve the lowest
647 lattice strains with garnet, in subgroup I1a the best fits were achieved by planes parallel to
648 {0001}. This does fit with the greater number of inclusions rotated around their *c*-axes for
649 ilmenite as compared to corundum (compare subgroup C1c, 1% of all corundum orientations,
650 with subgroup I1c, 7% of all ilmenite orientations).

651 In group I3, the only good alignment is $\{33\text{-}60\}_{\text{Ilm}} \| \{888\}_{\text{Grt}}$ (lattice strain -0.01). The fact that
652 these are the only fixed planes of a rotational statistical COR may suggest that this high-indexed
653 planar relationship is actually favorable.

654 **Evaluation.** The calculated lattice strains and plane indices are not very effective at explaining
655 the CORs observed. Although at least one set of low-indexed inclusion planes usually fits well
656 with garnet for each group/subgroup, the results do not reflect the observed relative frequencies
657 of each COR and cannot explain why a particular COR is specific or statistical. An interface-
658 scale factor not addressed here is the nature of bonding across the host–inclusion interface.
659 Strong (and thus energetically favorable) bonds between atoms preferentially exposed at certain
660 orientations of interface planes could encourage specific relationships that appear unfavorable
661 due to lattice strain alone.

662 It appears that the continuation of symmetry elements between host and inclusion has a strong
663 influence on CORs. Many CORs with only a single set of well-fitting planes are nonetheless
664 specific rather than rotational statistical, and the same direction (the {11-20} pole) is the axis of a

665 rotational statistical COR for both trigonal phases, despite the fact that for corundum in
666 particular, other planes would theoretically have better fits. One possible factor which could
667 favor continuation of symmetry elements is the minimization of elastic strain energy between
668 host and inclusion at a larger scale than individual lattice planes, controlling CORs by the
669 interaction of host and inclusion elastic properties. These do have several characteristics similar
670 to statistical CORs. The {111} planes in garnet, populated by rutile *a*-axes of the subgroup R3a
671 rotational statistical COR, are planes of constant garnet stiffness. Regions of shallow gradients in
672 elastic properties exist around low-indexed garnet crystallographic directions, coinciding with
673 axis relationships where dispersion of rutile directions is seen. This explanation has difficulty
674 explaining the importance of the rutile <103> direction however, as this is a direction of neither
675 minimum nor maximum stiffness in rutile, and the resulting conical distribution of the stiff
676 (relative to garnet) rutile *c*-axis does not follow contours of constant garnet stiffness.

677 **Implications**

678 This work shows that multiple coexisting CORs and statistical CORs between host and
679 inclusions are not an isolated quirk of rutile inclusions in garnet. Studies based on relatively
680 small numbers of inclusion orientations have likely overlooked statistical CORs and
681 underestimated the true variety of CORs present, with implications for interpretations of
682 inclusion origins.

683 It is essential to test the above hypothesis and discover how widespread the features of CORs
684 identified in the Wirtbartl garnets are. Future studies of host–inclusion systems should involve
685 large numbers of measurements in order to accommodate the concept of statistical CORs and
686 obtain a representative picture of the frequency of the different CORs detected. EBSD is the

687 optimum method to achieve COR characterization within a reasonable timeframe. Context from
688 EBSD measurements greatly increases the value of any TEM data obtained on individual
689 inclusions and avoids unrepresentative conclusions.

690 The CORs defined for a given sample should be guided by the amount of data available, the
691 limitations of the methods employed, the aims of the study, and prior knowledge of the system.
692 As decisions about how to describe a distribution of inclusion orientations can influence the way
693 a dataset is presented, future studies should explicitly discuss their reasons for defining each
694 COR reported. Failure to do this could obscure important aspects of the data.

695 Sufficiently large numbers of measurements of inclusion orientations provide information on
696 many different parameters: which - and how many - CORs each inclusion phase assumes, the
697 relative frequencies of these CORs, whether these CORs are specific or statistical, and the
698 amount of rotation and dispersion of each statistical COR. A survey of rutile inclusion CORs in
699 garnet from multiple localities suggests these parameters are likely affected by processes of
700 inclusion formation / incorporation and/or variables such as pressure, temperature, cooling rate,
701 composition, interface geometry, nucleation rate, or growth rate. An improved understanding of
702 the small and large scale processes controlling the development of the full range of host-
703 inclusion CORs could deliver information not only about the origins of the inclusions involved
704 but also the conditions at the time of formation.

705 It is currently not possible to predict the favorability of particular CORs from knowledge of host
706 and inclusion crystal lattices. A simple model involving the minimization of misfits between
707 parallel sets of host and inclusion lattice planes could not fully explain the frequency or
708 characteristics of the CORs observed in the Wirtbartl samples, implying that unaccounted for

interface-scale factors (e.g. atomic bonding), long range interactions such as elastic strain and/or the formation mechanisms of the inclusions may be important factors. Combined EBSD and TEM studies of systems where the origin of inclusions is independently known are necessary to determine the influence of inclusion formation processes on the resulting CORs. Improved computer models of the 3D atomic structure of interfaces will make it possible to probe the influence of other variables on the favorability of different CORs. An ultimate goal would be to be able to divide inclusions into COR groups based on physical characteristics of their interfaces and genetic considerations.

Acknowledgements

The authors acknowledge funding by the University of Vienna doctoral school IK052 Deformation of Geological Materials (DOGMA) and the project of the Austrian Science Fund (FWF): I471-N19, as part of the international DFG-FWF funded research network FOR741-DACH. Dr. Helen M. Lang is thanked for providing information about the presumed source rocks of the Idaho star garnets.

References

Ague, J.J., and Eckert Jr., J.O. (2012) Precipitation of rutile and ilmenite needles in garnet: Implications for extreme metamorphic conditions in the Acadian Orogen, U.S.A. American Mineralogist, 97, 840–855.

Amouric, M., Baronnet, A., Nahon, D., and Didier, P. (1986) Electron microscopic investigations of iron oxyhydroxides and accompanying phases in lateritic iron-crust pisolites. Clays and Clay Minerals, 34, 45–52.

730 Bachmann, F., Hielscher, R., and Schaeben, H. (2010) Texture analysis with MTEX- Free and
731 open source software toolbox. Solid State Phenomena, 160, 63–68.

732 Balluffi, R.W., Allen, S., and Carter, W.C. (2005) Kinetics of Materials, 674 p. John Wiley &
733 Sons, Hoboken.

734 Bestmann, M., Habler, G., Heidelbach, F., and Thoni, M. (2008) Dynamic recrystallization of
735 garnet and related diffusion processes. Journal of Structural Geology, 30, 777–790.

736 Brearley, A.J., and Champness, P.E. (1986) Magnetite exsolution in almandine garnet.
737 Mineralogical Magazine, 50, 621–633.

738 Bursill, L.A., and Withers, R.L. (1979) On the multiple orientation relationships between
739 hematite and magnetite. Journal of Applied Crystallography, 12, 287–294.

740 Burton, K.W. (1986) Garnet-quartz intergrowths in graphitic pelites: the role of the fluid phase.
741 Mineralogical Magazine, 50, 611–620.

742 Frazer, C.S., Dickey, E.C., and Sayir, A. (2001) Crystallographic texture and orientation variants
743 in Al2O3-Y3Al5O12 directionally solidified eutectic crystals. Journal of Crystal Growth,
744 233, 187–195.

745 Glassley, W.E., Korstgård, J.A., Ensen, K.S., and Platou, S.W. (2014) A new UHP metamorphic
746 complex in the ~1.8 Ga Nagssugtoqidian Orogen of west Greenland. American
747 Mineralogist, 99, 1315–1334.

748 Gou, L., Zhang, C., Zhang, L., and Wang, Q. (2014) Precipitation of rutile needles in garnet from
749 sillimanite-bearing pelitic granulite from the Khondalite Belt, North China Craton.
750 Chinese Science Bulletin, 59, 4359–4366.

751 Green II, H.W., Dobrzhinetskaya, L., Riggs, E.M., and Jin, Z.-M. (1997) Alpe Arami: A
752 peridotite massif from the mantle transition zone? Tectonophysics, 279, 1–21.

753 Gregurek, D., Abart, R., and Hoinkes, G. (1997) Contrasting Eoalpine P-T evolutions in the
754 southern Koralpe, Eastern Alps. Mineralogy and Petrology, 60, 61–80.

755 Griffiths, T.A., Habler, G., Rhede, D., Wirth, R., Ram, F., and Abart, R. (2014) Localization of
756 submicron inclusion re-equilibration at healed fractures in host garnet. Contributions to
757 Mineralogy and Petrology, 168, 1–21.

758 Guinel, M.J.-F., and Norton, M.G. (2006) The origin of asterism in almandine-pyrope garnets
759 from Idaho. Journal of Materials Science, 41, 719–725.

760 Habler, G., and Thöni, M. (2001) Preservation of Permo–Triassic low-pressure assemblages in
761 the Cretaceous high-pressure metamorphic Saualpe crystalline basement (Eastern Alps,
762 Austria). Journal of Metamorphic Geology, 19, 679–697.

763 Habler, G., Thöni, M., and Miller, C. (2007) Major and trace element chemistry and Sm-Nd age
764 correlation of magmatic pegmatite garnet overprinted by eclogite-facies metamorphism.
765 Chemical Geology, 241, 4–22.

766 Hatert, F., Baijot, M., Philippo, S., and Wouters, J. (2010) Qingheiite-(Fe2+), Na2Fe2+MgAl(PO
767 4)3, a new phosphate mineral from the Sebastião Cristino pegmatite, Minas Gerais,
768 Brazil. European Journal of Mineralogy, 22, 459–467.

769 Hielscher, R., Schaeben, H., and Siemes, H. (2010) Orientation distribution within a single
770 hematite crystal. Mathematical Geosciences, 42, 359–375.

771 Howe, J.M. (1997) Interfaces in Materials: Atomic Structure, Thermodynamics and Kinetics of
772 Solid-Vapor, Solid-Liquid and Solid-Solid Interfaces. John Wiley & Sons, Hoboken.

773 Hwang, S.L., Yui, T.F., Chu, H.T., Shen, P., Schertl, H.P., Zhang, R.Y., and Liou, J.G. (2007)
774 On the origin of oriented rutile needles in garnet from UHP eclogites. Journal of
775 Metamorphic Geology, 25, 349–362.

776 Hwang, S.-L., Yui, T.-F., Chu, H.-T., Shen, P., Zhang, R.-Y., and Liou, J.G. (2011) An AEM
777 study of garnet clinopyroxenite from the Sulu ultrahigh-pressure terrane: formation
778 mechanisms of oriented ilmenite, spinel, magnetite, amphibole and garnet inclusions in
779 clinopyroxene. Contributions to Mineralogy and Petrology, 161, 901–920.

780 Hwang, S.L., Shen, P., Chu, H.T., Yui, T.F., and Iizuka, Y. (2013) A TEM study of the oriented
781 orthopyroxene and forsterite inclusions in garnet from Otrøy garnet peridotite, WGR,
782 Norway: new insights on crystallographic characteristics and growth energetics of
783 exsolved pyroxene in relict majoritic garnet. Journal of Metamorphic Geology, 31, 113–
784 130.

785 Hwang, S.-L., Shen, P., Chu, H.-T., Yui, T.-F., and Iizuka, Y. (2015) Origin of rutile needles in
786 star garnet and implications for interpretation of inclusion textures in ultrahigh-pressure
787 metamorphic rocks. Journal of Metamorphic Geology, 33, 249–272.

788 Lang, H.M., Johnson, S.E., and Largent, K.J. (2014) Use of garnet zoning and pseudosection
789 modeling to constrain the P-T path of metapelitic tectonites in the snow peak area,
790 northern Idaho. Geological Society of America Abstracts with Programs, 46, 140.

791 Miller, C., and Thöni, M. (1997) Eo-Alpine eclogitisation of Permian MORB-type gabbros in the
792 Koralpe (Eastern Alps, Austria): New geochronological, geochemical and petrological
793 data. Chemical Geology, 137, 283–310.

794 Miller, C., Thöni, M., Konzett, J., Kurz, W., and Schuster, R. (2005) Eclogites from the Koralpe
795 and Saualpe type-localities, eastern Alps, Austria. Mitteilungen der Österreichischen
796 Mineralogischen Gesellschaft, 227–263.

797 Miller, C., Zanetti, A., Thöni, M., and Konzett, J. (2007) Eclogitisation of gabbroic rocks:
798 Redistribution of trace elements and Zr in rutile thermometry in an Eo-Alpine subduction
799 zone (Eastern Alps). Chemical Geology, 239, 96–123.

800 Moore, P., and lto, J. (1979) Alluaudites, wyllieites, arrojadites: crystal chemistry and
801 nomenclature. Mineralogical Magazine, 43, 227–235.

802 Mposkos, E.D., and Kostopoulos, D.K. (2001) Diamond, former coesite and supersilicic garnet
803 in metasedimentary rocks from the Greek Rhodope: a new ultrahigh-pressure
804 metamorphic province established. Earth and Planetary Science Letters, 192, 497–506.

Proyer, A., Habler, G., Abart, R., Wirth, R., Krenn, K., and Hoinkes, G. (2013) TiO2 exsolution from garnet by open-system precipitation: evidence from crystallographic and shape preferred orientation of rutile inclusions. Contributions to Mineralogy and Petrology, 166, 211–234.

Ram, F., Zaefferer, S., Jäpel, T., and Raabe, D. (2015) Error analysis of the crystal orientations and disorientations obtained by the classical electron backscatter diffraction technique. Journal of Applied Crystallography, 48.

Ruiz-Cruz, M.D., and Sanz de Galdeano, C. (2013) Coesite and diamond inclusions, exsolution microstructures and chemical patterns in ultrahigh pressure garnet from Ceuta (Northern Rif, Spain). Lithos, 177, 184–206.

Schmid, S.M., Fügenschuh, B., Kissling, E., and Schuster, R. (2004) Tectonic map and overall architecture of the Alpine orogen. Eclogae Geologicae Helvetiae, 97, 93–117.

Schuster, R., and Stüwe, K. (2008) Permian metamorphic event in the Alps. Geology, 36, 603–606.

Sugiyama, K., Nakai, M., AYoshikawa, and Fukuda, T. (2009) Microstructure and crystal chemistry of eutectic Al2O 3/Y3Al5O12 Fibers Modified by the Partial Substitution of Sc2O3 for Al2O 3. High Temperature Materials and Processes, 28, 89–95.

Tenczer, V., and Stüwe, K. (2003) The metamorphic field gradient in the eclogite type locality, Koralpe region, Eastern Alps. Journal of Metamorphic Geology, 21, 377–393.

824 Tenczer, V., Powell, R., and Stüwe, K. (2006) Evolution of H2O content in a polymetamorphic
825 terrane: the Plattengneiss Shear Zone (Koralpe, Austria). Journal of Metamorphic
826 Geology, 24, 281–295.

827 Thöni, M. (2006) Dating eclogite-facies metamorphism in the Eastern Alps - Approaches,
828 results, interpretations: A review. Mineralogy and Petrology, 88, 123–148.

829 Thöni, M., and Jagoutz, E. (1992) Some new aspects of dating eclogites in orogenic belts: Sm-
830 Nd, Rb-Sr, and Pb-Pb isotopic results from the Austroalpine Saualpe and Koralpe type-
831 locality (Carinthia/Styria, southeastern Austria). Geochimica et Cosmochimica Acta, 56,
832 347–368.

833 Thöni, M., and Miller, C. (2000) Permo-triassic pegmatites in the eo-alpine eclogite-facies
834 Koralpe complex, Austria: Age and magma source constraints from mineral chemical,
835 Rb-Sr and Sm-Nd isotope data. Schweizerische Mineralogische und Petrographische
836 Mitteilungen, 80, 169–186.

837 ——— (2009) The "Permian event" in the Eastern European Alps: Sm–Nd and P–T data
838 recorded by multi-stage garnet from the Plankogel unit. Chemical Geology, 260, 20–36.

839 Thöni, M., Miller, C., Zanetti, A., Habler, G., and Goessler, W. (2008) Sm-Nd isotope
840 systematics of high-REE accessory minerals and major phases: ID-TIMS, LA-ICP-MS
841 and EPMA data constrain multiple Permian-Triassic pegmatite emplacement in the
842 Koralpe, Eastern Alps. Chemical Geology, 254, 216–237.

Van Roermund, Drury, Barnhoorn, and De Ronde (2000) Super-silicic garnet microstructures from an orogenic garnet peridotite, evidence for an ultra-deep (>6 GPa) origin. Journal of Metamorphic Geology, 18, 135–147.

West, N., Foley, N., and Evans, J. (2005) Garnet gravels and their source rocks: a comparative study of garnet resources of the Emerald Creek area, Idaho. Geological Society of America Abstracts with Programs, 37, 63.

Xu, H., Zhang, J., Zong, K., and Liu, L. (2015) Quartz exsolution topotaxy in clinopyroxene from the UHP eclogite of Weihai, China. Lithos, 226, 17–30.

Ye, K., Cong, B., and Ye, D. (2000) The possible subduction of continental material to depths greater than 200□km. Nature, 407, 734–736.

Zhang, J.F., Xu, H.J., Liu, Q., Green, H.W., and Dobrzhinetskaya, L.F. (2011) Pyroxene exsolution topotaxy in majoritic garnet from 250 to 300 km depth. Journal of Metamorphic Geology, 29, 741–751.

Zhang, R.Y., and Liou, J.G. (2003) Clinopyroxenite from the Sulu ultrahigh-pressure terrane, eastern China: Origin and evolution of garnet exsolution in clinopyroxene. American Mineralogist, 88, 1591–1600.

Figure Captions

FIGURE 1. Transmitted plane polarized light micrographs of thin sections show concentric (**a**) and sector (**b**) zoning in Wirtbartl metapegmatite garnets, defined by variations in inclusion abundances, grain sizes and habits. Inclusion trails with bleaching zones (Griffiths et al. 2014) crosscut the zoning. Oscillatory zoning visible at bottom right of (**a**).

FIGURE 2. Inclusion EBSD measurement domains A (**a-d**) and B (**e-h**). Optical overviews of each domain [(**a**) and (**e**)] show the regions from which inclusion orientations were obtained (black dashed lines), the number of measurements made, and the positions of optical close-ups [(**c**) and (**g**), pink rectangles] and BSE images [(**d**) and (**h**), orange rectangles]. (**b**) and (**f**) provide optical context, the areas shown in (**a**) and (**e**) are indicated by yellow polygons.

FIGURE 3. The orientation distribution function (ODF) of all measured rutile inclusion <001> directions, plotted relative to a fixed garnet orientation (antipodal, equal angle, upper hemisphere pole figure). The halfwidth (HW) and intensity of the ODF are indicated to the right of the pole figure, and the ODF color scale is shown below. Garnet crystallographic directions are indicated by colored squares and triangles, see legend above the pole figure. Colored small circles indicate rutile *c*-axis criteria used to define the groups of rutile inclusions set out in table 1: R1 = dark grey, R1* = light blue, R3 = red. Group R2 *c*-axis maxima are hidden by overlying garnet <111> symbols.

FIGURE 4. EBSD data from rutile inclusions in groups R1 and R1* plotted relative to a fixed garnet orientation. Both plots are antipodal, equal angle, upper hemisphere pole figures. Garnet directions are indicated by colored squares and triangles, see legend in figure 3. (**a**) Orientation of rutile <001> (red) and <100> (blue) directions for group R1. Dark grey small circles have a

radius of 5°. (**b**) Histogram showing the distribution of misorientation angles (in degrees) between rutile *c*-axes and garnet <110> directions for groups R1 and R1*. Bins are 1° wide. (**c**) Orientation of rutile <001> directions for groups R1 (red) and R1* (light blue). Also plotted is an ODF of group R1* <100> directions (color scale as in fig. 3). The halfwidth (HW), minimum and maximum intensity of the ODF are indicated to the right of the pole figure. Small circles of 5° (dark grey) and 22° (light blue) are drawn around the garnet [0-11] direction. A fourfold rotation was used to combine symmetrically equivalent inclusion data into a single pole figure quadrant (see section 'pole figure plot construction').

FIGURE 5. EBSD data from rutile inclusions in subgroups R3a and R3b plotted relative to a fixed garnet orientation. All plots are antipodal, equal angle, upper hemisphere pole figures. Garnet directions are indicated by colored squares and triangles, see legend in figure 3. A fourfold rotation was used to combine inclusion data from symmetrically equivalent garnet directions into a single pole figure quadrant for all plots (see section 'pole figure plot construction'). Red small circles are at inclination angles of 26° and 31° from garnet [111]. (**a**) The orientation of rutile <001> (red, **i**+**ii**), <100> (blue, **i**) and <103> (blue, **ii**) directions for subgroup R3a (legend above each figure). Black small circles are at inclination angles of 62° and 90° to garnet [111] for (**i**) and 38° and 55° to garnet [111] for (**ii**). (**b**) The orientation of rutile <001> (red, **i**+**ii**) and <100> (blue, **i**) directions and {101} (blue, **ii**) plane poles for subgroup R3b (legend above each figure). Black small circles are at inclination angles of 62° and 90° to garnet [111] for (**i**).

FIGURE 6. EBSD data from corundum inclusions in groups C1 (**a**), C2 (**b**) and C4 (**c**) plotted relative to a fixed garnet orientation. Poles to corundum {0001} planes are indicated in all plots as red circles. In addition, the left column of plots (**i**) shows corundum {11-20} plane poles

(blue) and the right column (**ii**) shows {10-10} poles (blue) for each group. All plots are antipodal, equal angle, upper hemisphere pole figures. Garnet directions are indicated by colored squares and triangles, see legend in figure 3. A fourfold rotation was used to combine inclusion data from symmetrically equivalent garnet directions into a single pole figure quadrant for all plots (see section 'pole figure plot construction'). Black small circles indicate (**a**) garnet {112} planes (**b**) a garnet {111} plane (**ci**) a garnet {111} plane and a cone inclined at 60° to garnet [111] and (**cii**) a garnet {111} plane and a cone inclined at 30° to garnet [111].

FIGURE 7. EBSD data from ilmenite inclusions in groups I1 (**a**), I2 (**b**) and I3 (**c**) plotted relative to a fixed garnet orientation. Poles to ilmenite {0001} planes are indicated in all plots as red circles. In addition, the left column of plots (**i**) shows ilmenite {11-20} plane poles (blue) and the right column (**ii**) shows {10-10} poles (blue). All plots are antipodal, equal angle, upper hemisphere pole figures. Garnet directions are indicated by colored squares and triangles, see legend in figure 3. A fourfold rotation was used to combine inclusion data from symmetrically equivalent garnet directions into a single pole figure quadrant for all plots (see section 'pole figure plot construction'). Black small circles indicate (**a**) garnet {112} planes (**b**) a garnet {111} plane (**ci**) a garnet {111} plane and a cone inclined at 60° to garnet [111] and (**cii**) a garnet {111} plane and a cone inclined at 30° to garnet [111].

FIGURE 8. Equal angle projection plot of rutile orientation data adapted from Hwang et al. (2007). The original plot is underlain by small circles at 28° and 33° to one garnet <111> direction (red continuous lines) and small circles at 57° and 90° to the same direction (blue dotted lines, dots 2° apart). Garnet <134> (orange triangles) and <112> (green triangles) directions in the (-11-1) garnet plane are plotted, and do not coincide with rutile *a*-axes a_1 or $a_3 - a_6$, which belong to rutile inclusions with *c*-axes (c_1 & $c_3 - c_6$) inclined on cones to garnet [-11-1]

(red small circles). Figure used by permission of John Wiley and Sons, from Hwang et al. (2007), Journal of Metamorphic Petrology, vol. 25, Fig. 3, p. 354.

This is a preprint, the final version is subject to change, of the American Mineralogist (MSA)
Cite as Authors (Year) Title. American Mineralogist, in press.
(DOI will not work until issue is live.) DOI: http://dx.doi.org/10.2138/am-2016-5442

Tables

TABLE 1. Relationships between crystallographic directions of rutile inclusions and host garnet

Group	rt *c*-axis ‖ grt <uvw>	N (gp.)	Largest subgroup(s)	(sub)group rt *a*-axis ‖ grt <uvw>	(sub)group rt {101} ‖ grt <uvw>	(sub)group rt <103> ‖ grt <uvw>	N (sgp.)
R1	grt <110> (±5°)	43	R1a	grt <111> (±5°) (1ax) grt <112> (±5°) (1ax)	-	-	39
R1*	grt <110> (>5°, <22°)	84	-	concentrated at grt <111> (1ax)	n.o.	n.o.	-
R2	grt <111>	4	R2a	grt <110> (1ax) grt <112> (1ax)	-	-	3
R3	Cone around grt <111> (28.5° ± 2.5)	103	R3a	1ax in grt {111} plane (±5°), avoid grt <110>	n.o.	grt <111> (±5°) (1ax)	80
			R3b	Never in grt {111} plane 1ax near grt <112>	grt <110> (1ax)	n.o.	14
RX	n.o.	16	-	n.o.	n.o.	n.o.	-

Notes: rt = rutile; grt = garnet; gp. = group; sgp = subgroup; n.o. = not observed. The largest subgroup in each group is detailed in this table. Additional subgroups with N ≥10 are also included. Where two orientation relationships are enough to define a specific COR, the other columns are left blank (-).The number of symmetrically equivalent crystallographic directions which follow each relationship is indicated (1ax = one direction, 2ax = 2 directions, no comment = all equivalent directions share the relationship).

TABLE 2. Relationships between crystallographic directions of corundum inclusions and host garnet

Group	crn *c*-axis ‖ grt <uvw>	N (gp.)	Largest subgroup	(sub)group crn *a*-axis ‖ grt <uvw>	(sub)group crn {10-10} pole ‖ grt <uvw>	N (sgp.)
C1	grt <112>	69	C1a	grt <111> (1ax) near grt <113> (2ax)	grt <110> (1ax) near grt <135> (2ax)	62
C2	grt <111>	56	C2a	grt <112>	grt <110>	53
C3	grt <100>	3	-	grt <110> (1ax)	grt <110> (1ax)	-
C4	in grt {111}	28	-	grt <111> (±5°)	1ax in grt {111} plane (±5°)	-
CX	n.o.	24	-	n.o.	n.o.	-

Notes: crn = corundum; grt = garnet; gp. = group; sgp = subgroup; n.o. = not observed. The largest subgroup in each group is detailed in this table. No additional subgroups with N ≥ 10 were found. The number of symmetrically equivalent crystallographic directions which follow each relationship is indicated (1ax = one direction, 2ax = 2 directions, no comment = all equivalent directions share the relationship).

960

TABLE 3. Relationships between crystallographic directions of ilmenite inclusions and host garnet

Group	ilm *c*-axis ‖ grt <uvw>	N (gp.)	Largest subgroup	(sub)group ilm *a*-axis ‖ grt <uvw>	(sub)group ilm {10-10} pole ‖ grt <uvw>	N (sgp.)
I1	grt <112>	28	I1a	grt <111> (1ax) near grt <113> (2ax)	grt <110> (1ax) near grt <135> (2ax)	21
I2	grt <111>	21	I2a	grt <112>	grt <110>	20
I3	in grt {111}	35	-	grt <111> (±5°)	1ax in grt {111} plane (±5°)	-
IX	n.o.	16	-	n.o.	n.o.	-

Notes: ilm = ilmenite; grt = garnet; gp. = group; sgp = subgroup; n.o. = not observed. The largest subgroup in each group is detailed in this table. No additional subgroups with N ≥ 10 were found. The number of symmetrically equivalent crystallographic directions which follow each relationship is indicated (1ax = one direction, 2ax = 2 directions, no comment = all equivalent directions share the relationship).

961

962

TABLE 4. Calculation of lattice strains for parallel sets of rutile and garnet planes determined using EBSD.

(Sub)group	CORs from EBSD (format: rt ‖ grt)	Lowest index planes (-0.04 ≤ ε ≤ 0.04) (format: rt ‖ grt)	ε	Best fit 1 : x d-spacing ratio (format: rt ‖ grt)	ε (1 : x d-spacing ratio)
R1a	{001}‖{110}	{003}‖{880}	0.04	{001}‖{330}	-0.08
	{100}‖{112} ***(1ax)***	**{100}‖{112}**	**0.03**	-	-
R1a / R1*	**{100}‖{111}** ***(1ax)***	**{200}‖{333}**	**-0.03**	-	-
R2a	{001}‖{111}	{003}‖{777}	-0.03	{001}‖{222}	0.12
	{100}‖{112} ***(1ax)***	**{100}‖{112}**	**0.03**	-	-
	{100}‖{110} ***(1ax)***	{004}‖{777}	0.02	{100}‖{220}	-0.12
R3a	**<103>‖<111>**	**<206>‖<111>**	**0.00**	-	-
	{405}‖{111}	{405}‖{13 13 13}	-0.02	{405}‖{12 12 12}	0.06
R3b	{001}‖{113}	{005}‖{6 6 18}	-0.02	{001}‖{113}	0.15
	{100}‖{112} ***(1ax)***	**{100}‖{112}**	**0.03**	-	-
	{101}‖{110}	{303}‖{10 10 0}	-0.01	{101}‖{330}	0.09

Notes: rt = rutile; grt = garnet; ε = calculated lattice strain. Lattice strains given to 2 decimal places, at this degree of precision errors in lattice constants used for the calculation are too small to affect the result. Bolded relationships are those where the target lattice strain can be achieved with a simple 1:x or 2:x d-spacing ratio. The number of symmetrically equivalent crystallographic directions which follow each relationship is indicated (1ax = one direction, no comment = all equivalent directions share the relationship).

963

964

TABLE 5. Calculation of lattice strains for parallel sets of corundum and garnet planes determined using EBSD.

(Sub)group	CORs from EBSD (format: crn ‖ grt)	Lowest index planes ($-0.04 \leq \varepsilon \leq 0.04$) (format: crn ‖ grt)	ε	Best fit 1 : x d-spacing ratio (format: crn ‖ grt)	ε (1 : x d-spacing ratio)
C1a	{0001}‖{112}	{0008}‖{336}	-0.03	{0003}‖{112}	0.08
	{11-20}‖{111} *(1ax)*	{4 4 -8 0}‖{11 11 11}	0.02	{11-20}‖{333}	-0.07
	{10-10}‖{110} *(1ax)*	**{10-10}‖{220}**	**-0.01**	-	-
C2a	**{0001}‖{111}**	**{0002}‖{111}**	**0.03**	-	-
	{11-20}‖{112}	**{11-20}‖{224}**	**-0.01**	-	-
	{10-10}‖{110}	**{10-10}‖{220}**	**-0.01**	-	-
C3	{0001}‖{001}	{0007}‖{006}	0.04	{0001}‖{001}	-0.12
	{11-20}‖{110} *(1ax)*	{22-40}‖{770}	-0.02	{11-20}‖{330}	0.13
	{10-10}‖{110} *(1ax)*	**{10-10}‖{220}**	**-0.01**	-	-
C4	{11-20}‖{111} *(1ax)*	{4 4 -8 0}‖{11 11 11}	0.02	{11-20}‖{333}	-0.07

Notes: crn = corundum; grt = garnet; ε = calculated lattice strain. Lattice strains given to 2 decimal places, at this degree of precision errors in lattice constants used for the calculation are too small to affect the result. Bolded relationships are those where the target lattice strain can be achieved with a simple 1:x or 2:x d-spacing ratio. The number of symmetrically equivalent crystallographic directions which follow each relationship is indicated (1ax = one direction, no comment = all equivalent directions share the relationship).

965

966

TABLE 6. Calculation of lattice strains for parallel sets of ilmenite and garnet planes determined using EBSD.

(Sub)group	CORs from EBSD (format: ilm ‖ grt)	Lowest index planes ($-0.04 \leq \varepsilon \leq 0.04$) (format: ilm ‖ grt)	ε	Best fit 1 : x d-spacing ratio (format: ilm ‖ grt)	ε (1 : x d-spacing ratio)
I1a	**{0001}‖{112}**	**{0003}‖{112}**	**0.01**	-	-
	{11-20}‖{111} *(1ax)*	{33-60}‖{888}	-0.01	{11-20}‖{333}	-0.14
	{10-10}‖{110} *(1ax)*	{50-50}‖{990}	-0.01	{10-10}‖{220}	-0.08
I2a	{0001}‖{111}	{0 0 0 13}‖{6 6 6}	0.03	{0002}‖{111}	-0.05
	{11-20}‖{112}	{5 5 -10 0}‖{9 9 18}	0.03	{11-20}‖{224}	-0.08
	{10-10}‖{110}	{50-50}‖{990}	-0.01	{10-10}‖{220}	-0.08
I3	{11-20}‖{111}	{33-60}‖{888}	-0.01	{11-20}‖{333}	-0.14

Notes: ilm = ilmenite; grt = garnet; ε = calculated lattice strain. Lattice strains given to 2 decimal places, at this degree of precision errors in lattice constants used for the calculation are too small to affect the result. Bolded relationships are those where the target lattice strain can be achieved with a simple 1:x or 2:x d-spacing ratio. The number of symmetrically equivalent crystallographic directions which follow each relationship is indicated (1ax = one direction, no comment = all equivalent directions share the relationship).

967

This is a preprint, the final version is subject to change, of the American Mineralogist (MSA)
Cite as Authors (Year) Title. American Mineralogist, in press.
(DOI will not work until issue is live.) DOI: http://dx.doi.org/10.2138/am-2016-5442

Figure 1

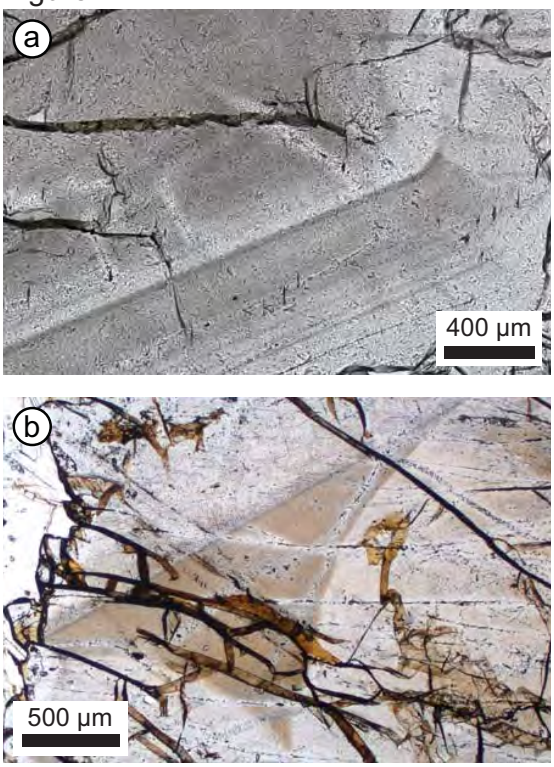

This is a preprint, the final version is subject to change, of the American Mineralogist (MSA)
Cite as Authors (Year) Title. American Mineralogist, in press.
(DOI will not work until issue is live.) DOI: http://dx.doi.org/10.2138/am-2016-5442

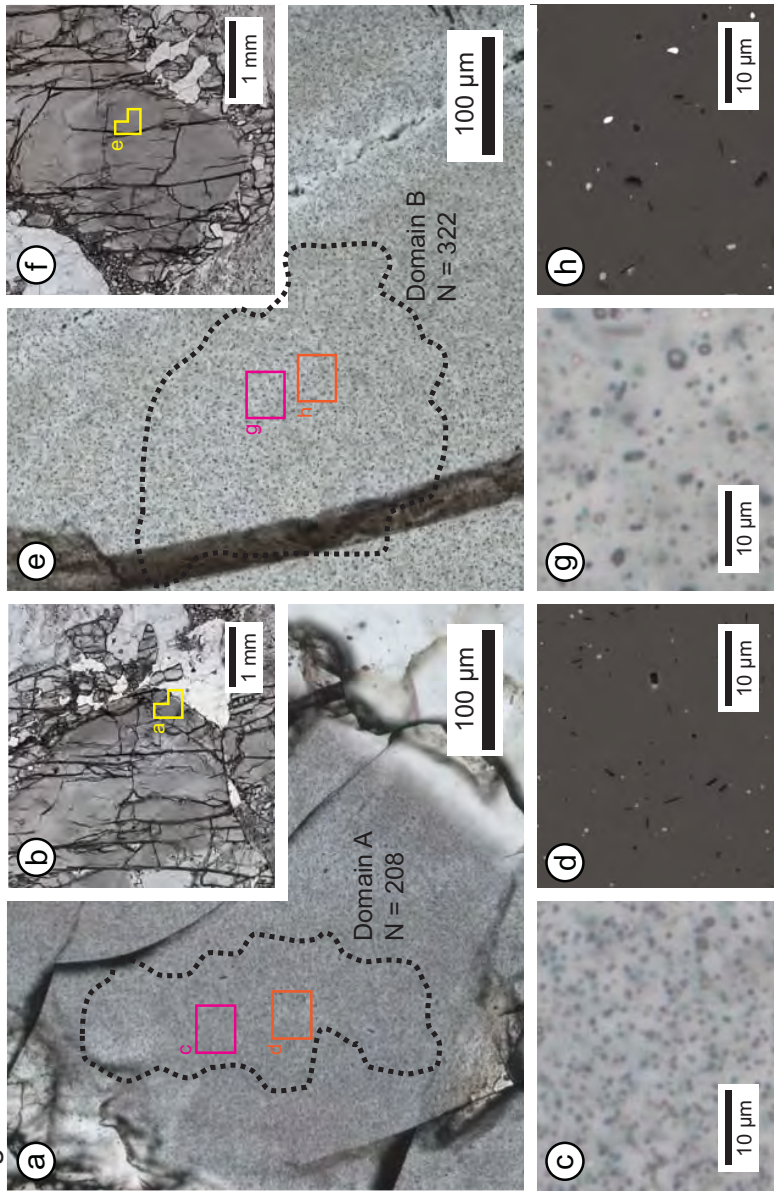

Figure 2

This is a preprint, the final version is subject to change, of the American Mineralogist (MSA)
Cite as Authors (Year) Title. American Mineralogist, in press.
(DOI will not work until issue is live.) DOI: http://dx.doi.org/10.2138/am-2016-5442

Figure 3

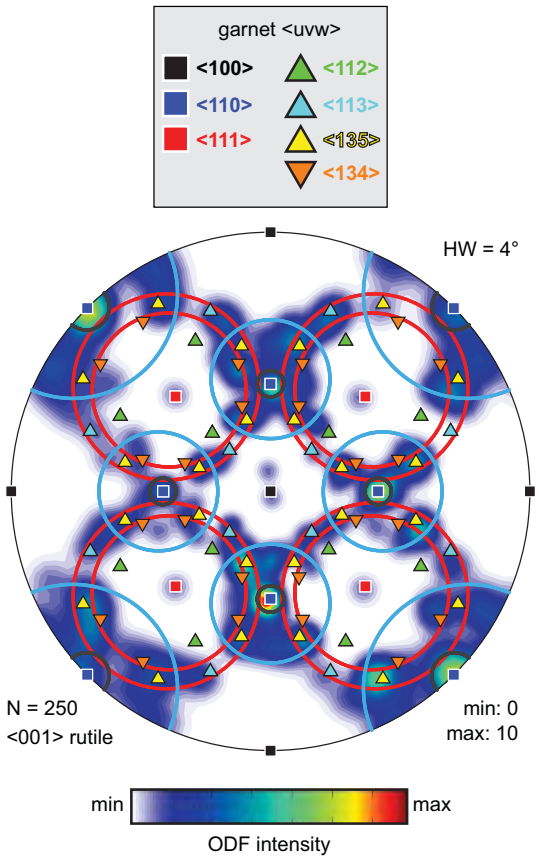

This is a preprint, the final version is subject to change, of the American Mineralogist (MSA)
Cite as Authors (Year) Title. American Mineralogist, in press.
(DOI will not work until issue is live.) DOI: http://dx.doi.org/10.2138/am-2016-5442

Figure 4

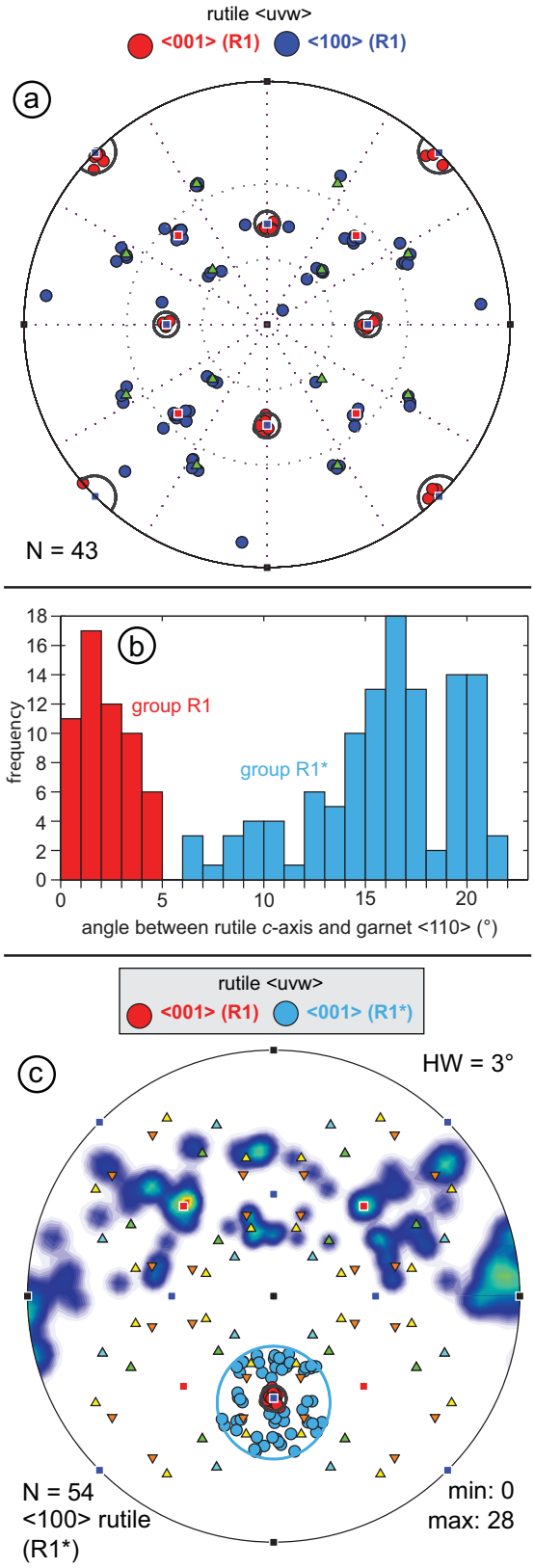

This is a preprint, the final version is subject to change, of the American Mineralogist (MSA)
Cite as Authors (Year) Title. American Mineralogist, in press.
(DOI will not work until issue is live.) DOI: http://dx.doi.org/10.2138/am-2016-5442

Figure 5

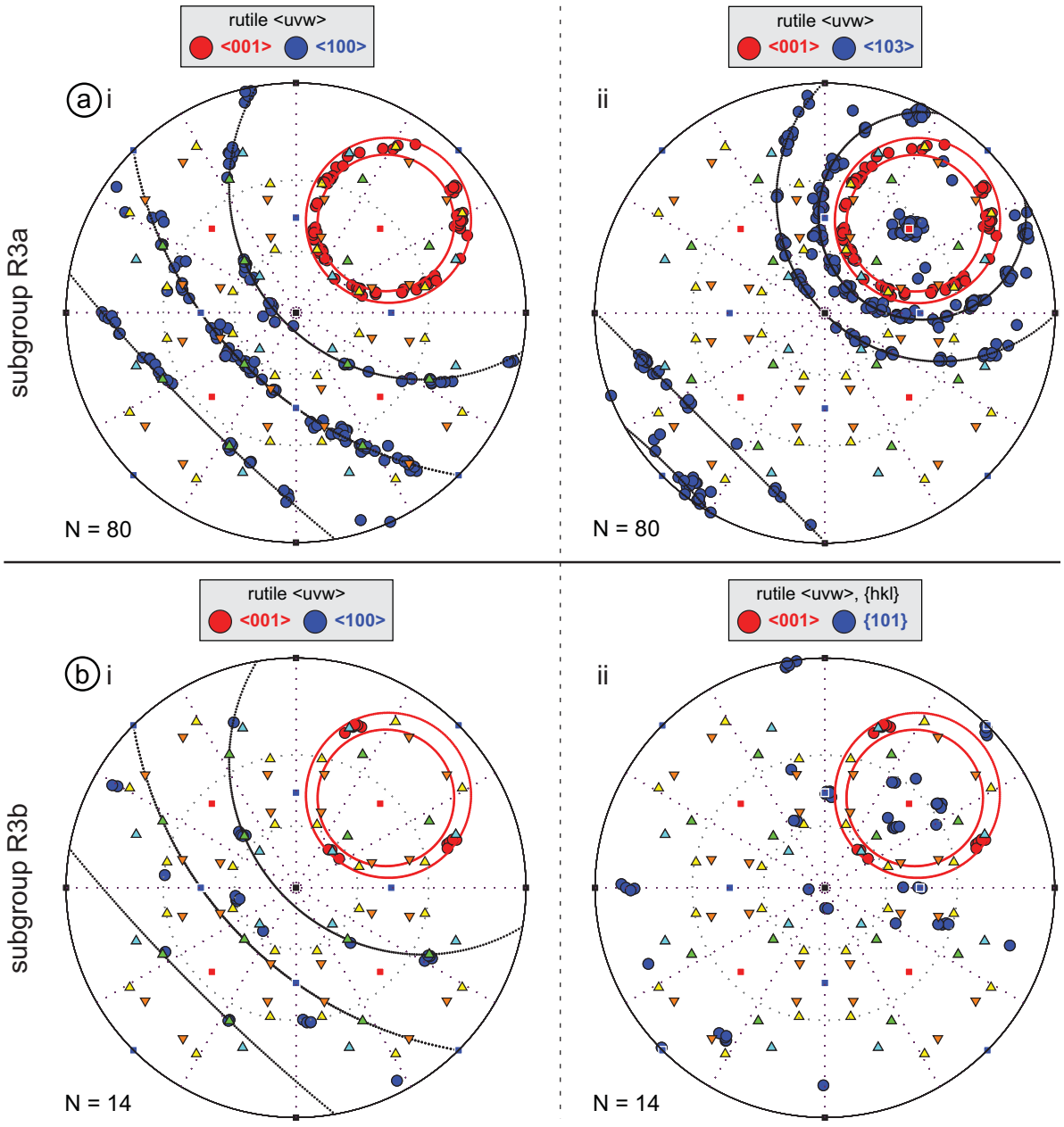

This is a preprint, the final version is subject to change, of the American Mineralogist (MSA)
Cite as Authors (Year) Title. American Mineralogist, in press.
(DOI will not work until issue is live.) DOI: http://dx.doi.org/10.2138/am-2016-5442

Figure 6

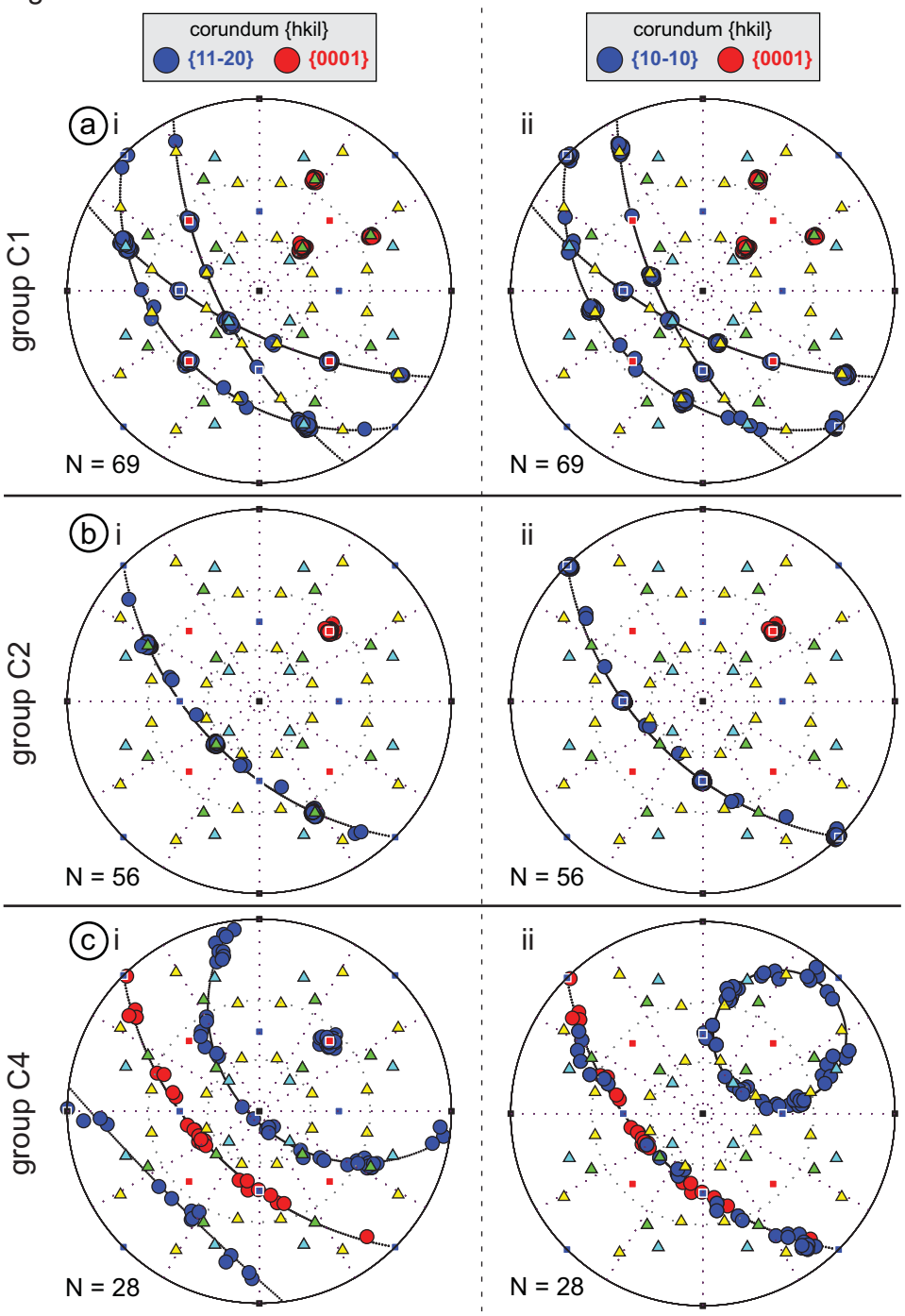

This is a preprint, the final version is subject to change, of the American Mineralogist (MSA)
Cite as Authors (Year) Title. American Mineralogist, in press.
(DOI will not work until issue is live.) DOI: http://dx.doi.org/10.2138/am-2016-5442

Figure 7

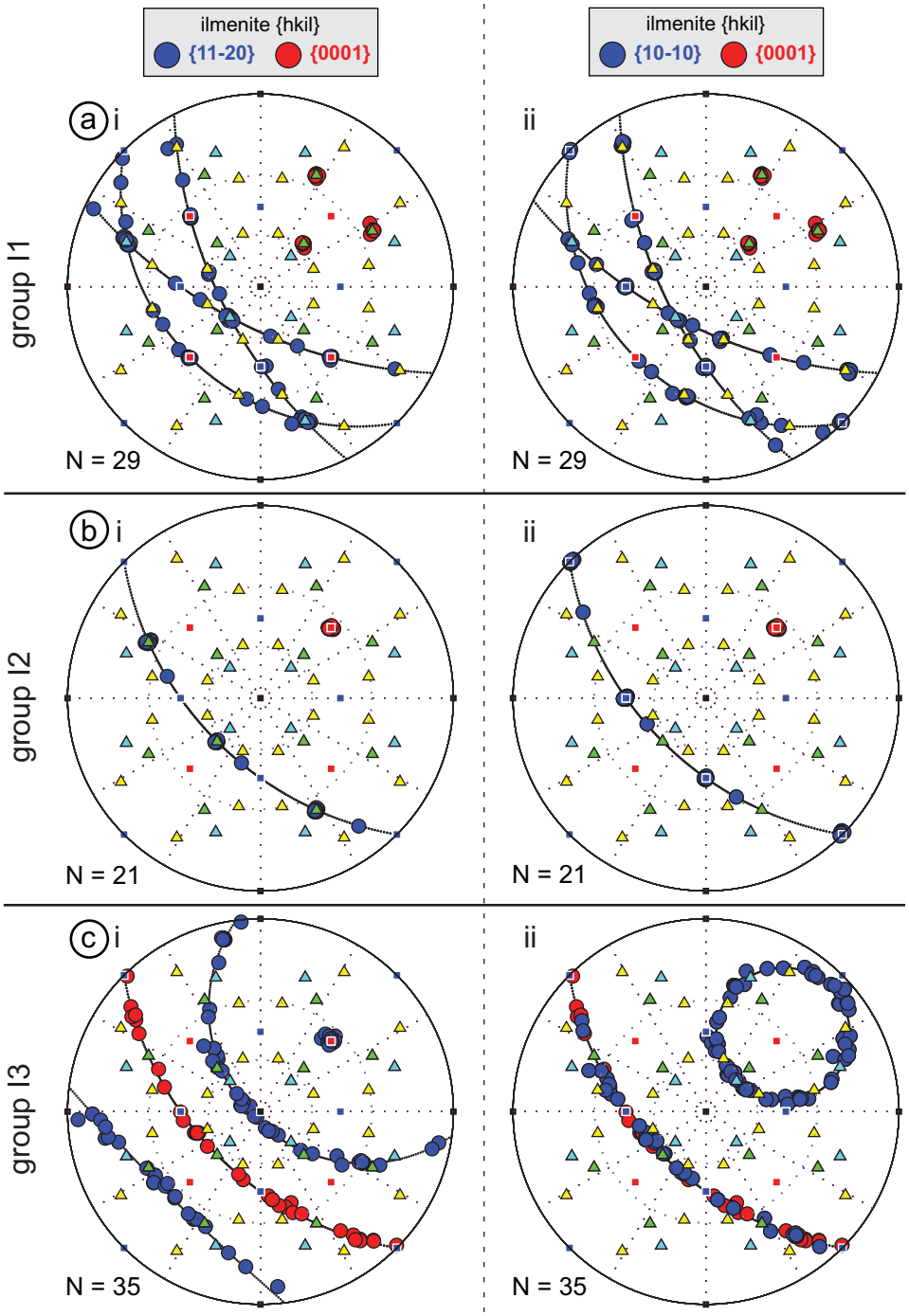

This is a preprint, the final version is subject to change, of the American Mineralogist (MSA)
Cite as Authors (Year) Title. American Mineralogist, in press.
(DOI will not work until issue is live.) DOI: http://dx.doi.org/10.2138/am-2016-5442

Figure 8